https://dx.doi.org/10.1016/j.ijplas.2023.103696

Crystal plasticity modelling of multi-stage deformation of ultra-thin sheets considering grain size effect and strain path change

Zhutian Xu [a,c], Rui Zhang [a,b], Linfa Peng [a,b,*], M.W. Fu [c,d,*]

[a] State Key Laboratory of Mechanical System and Vibration, Shanghai Jiao Tong University, Shanghai 200240, PR China

[b] Shanghai Key Laboratory of Digital Manufacture for Thin-Walled Structures, Shanghai Jiao Tong University, Shanghai 200240, PR China

[c] Department of Mechanical Engineering, Research Institute for Advanced Manufacturing, The Hong Kong Polytechnic University, Hung Hom, Kowloon, Hong Kong

[d] PolyU Shenzhen Research Institute, No. 18 Yuexing Road, Nanshan District, Shenzhen, PR China

[*] Corresponding author. E-mail address: penglinfa@sjtu.edu.cn (L.F. Peng)

[**] Corresponding author. E-mail address: mmmwfu@polyu.edu.hk (M.W. Fu)

Abstract

Multi-stage microforming is increasingly used in manufacturing of the miniaturized parts with complex structures and geometries. Optimization design of this type of manufacturing process, however, is still challenging due to its unknown intrinsic nature of the process. In the multi-stage deformation and microforming, the size effect (SE), the strain path change (SPC), and the intragranularly misoriented grain boundary (IMGB) generated in previous forming stage, are the main factors governing the deformation behaviors of ultra-thin sheets. To gain thorough insights into their influences on deformation and elucidate the associated micro-scaled mechanisms, SS 316L ultra-thin sheets with the thickness of 0.1 mm and different mean grain sizes ($\bar{d}$) were used for two-stage tensile tests under the conditions with distinct pre-strain ε_{pre} and intersection angle θ_{SPC} (the angle between the previous loading direction and subsequent one). Mechanical tests reveal that increasing ε_{pre} and θ_{SPC} reduces the yield stress and hardening rate in SPC tension, but this reduction gets smaller after increasing $\bar{d}$. This is because more IMGBs with complex pattern are formed in relatively large grains, raising the permanent deformation resistance inside grains in subsequent tension. To model the IMGB-induced hardening, the SPC-induced softening, and the SE-induced concurrent facilitations to the hardening and softening, an enhanced crystal plasticity constitutive relation was established. The physical essence that IMGB obstructs dislocation movement, is used to model the IMGB-induced hardening based on the interactions between the main slip planes and IMGBs. The hardening facilitation caused by increasing grain size is implicitly incorporated in determining the saturated slip resistance. Modelling of the SPC-induced softening is based on the high Schmid

factor grain fraction and its influences are governed by pre-strain and the defined SPC parameter. The softening facilitation caused by coarsening grains is modelled in establishing the initial slip resistance in SPC deformation. The proposed simulation procedure and constitutive relationship help with accurately predicting the mechanical response and microstructure evolution in micro-scaled SPC deformation, and also provide a basis for modelling and design of the multi-stage microforming of complex miniaturized parts.

Keywords

Size effect, Strain path change, Crystal plasticity, Micro-scaled deformation, Intragranularly misoriented grain boundary

1. Introduction

Micro sheet forming technology has been emergingly used in manufacturing of micro metal parts (Fu and Chan, 2013; Xu et al., 2020). With the increasing demands for weight lightening and product miniaturization, this technology has been facing various challenges including damage and fracture, anisotropy-related defect, and low dimensional accuracy, especially for the ultra-thin metallic sheets (Peng et al., 2014; Zheng et al., 2022). Multi-stage microforming is proposed to address these issues, because it not only has the advantages of traditional forming, such as high efficiency and low cost, but also fully uses the formability of sheet metals in stage-by-stage deformation (Bong et al., 2017; Zhang et al., 2021a). However, due to the coupled influences of grain size effect (SE) and strain path change (SPC) (Zhang et al., 2021b), high-fidelity modelling of the process is a challenging issue. Additionally, there are only several grains accommodating the main deformation in some critical regions of microparts. The product quality thus turns out to be strongly dependent on individual grains' deformation (Li et al., 2022b; Tang et al., 2020). Furthermore, those critical structures fabricated via complex forming procedures generally undergo the deformation with varying strain paths. The deformation-induced anisotropy generated in the previous process makes grains' mechanical responses more difficult to be predicted in subsequent deformation (Qin et al., 2019; Zaman et al., 2018). Therefore, the development of an accurate constitutive model based on the micro-scaled deformation mechanisms is crucial for the application of multi-stage microforming.

After the scaling down of workpiece, conventional knowledges of macro-scaled manufacturing may not be fully valid and thus cannot be directly leveraged to this downscaled fabrication scenario. In microforming, the SE strongly affects material's flow stress (Keller and Hug, 2017), springback (Xu et al., 2018), fracture (Crystal and Schuh, 2021), and product qualities (Tang et al., 2020). Notably, Lai et al. (2008) found

that the initial yield stress and flow stress of copper sheets were decreased with the increase of grain size or the decrease of sample thickness. This grain-size-dependent stress-strain relationship can be well described by the Hall-Petch relation (Armstrong, 1961; Hall, 1951; Petch, 1953) in the surface layer model (SLM). The SLM assumes that the grains in the external surfaces of workpieces are less constrained comparing with the inner ones (Engel and Eckstein, 2002; Geiger et al., 2001). With the increase of size factor, a ratio between the mean grain diameter and sample thickness, the fraction of surface layer is increased, leading to the decrease of flow stress. Xu et al. (2015) used the Holmberg and Marciniak methods to investigate the forming limit curves (FLCs) of copper sheets with different thicknesses and grain sizes. They found that the FLCs were shifted down by increasing size factor and well predicted by the extended GTN-Thomason model embedded with the SLM. Zheng et al. (2020) carried out the progressive micro pin forming of brass sheets, and revealed that the undesirable defects and surface roughness were increased with size factor. Peng et al. (2016) studied the micro-scaled friction behaviors, and attributed the surface quality deterioration to the transformation from adhesive friction to ploughing friction after increasing grain size. The SE-affected mechanical behaviors have been extensively studied, but their micro-scaled intrinsic mechanisms have not yet been fully revealed and well considered in modelling, especially for the practically used polycrystalline metallic materials.

Investigations on the strain-path-dependent mechanical behaviors are generally classified into two categories. For the first one, strain path is fully reversed in subsequent loading. The cyclic tension-compression (Yoshida et al., 2002), reversal bending (Zhang et al., 2020a), and reversal shearing (Thuillier and Manach, 2009) are usually used to study the Bauschinger effect (Chun et al., 2002). For the other, subsequent loading direction is intersected with previous stretching direction at a certain angle (0~90°) (Kim and Yin, 1997), which represents common SPC in complex sheet forming and is widely used to study the multi-stage deformation. The SPC has been validated to strongly affect material's deformation and forming behaviors (Chen et al., 2021; Schlosser et al., 2019). For instance, Wi et al. (2020) studied the mechanical responses of TRIP1180 steel and found that the second stage tensile stress along rolling direction (RD) was higher than the monotonic flow stress along transverse direction (TD) in previous stretching. Mánik et al. (2015) confirmed that the stress-strain curves of AA1050 sheets in the second stage stretching in TD were higher than those obtained in previous rolling along RD. Both curves gradually converged after more straining, which was similar to the observation from the research done by Holmedal et al. (2008). Moreover, Wen et al. (2015) explored the deformation behaviors of Mg alloy sheets via two-stage SPC tensile tests where the second stage tensile stress was smaller than the monotonic one. This deviation was increased with the intersection angle between two loading directions, which agreed with the studies using DP steel (Ha et al., 2017). Barlat

et al. (2011) developed a homogeneous anisotropic hardening model to describe the aforementioned hardening or softening behaviors in SPC loading. They proposed a “a microstructure history deviator” to characterize the yield surface variation (Liao et al., 2017). Based on this model, He et al. (2018) predicted the second stage flow stress of AZ31 sheets by using CPB06 yield function, and Herault et al. (2021) modelled the DP600’s softening behavior with Yld2000 yield criterion. Although these models have been used to describe the SPC-affected deformation behaviors, they are still challenged by unstable prediction (Qin et al., 2017), high experimental and computational cost (Ha et al., 2013; Lee et al., 2015). Previous researches manifest that the specific influences of SPC on deformation are dependent on the grain-level microstructures in microforming. Incorporating the related intrinsic mechanisms thus becomes a must for the modelling of micro-scaled SPC deformation.

Multi-stage microforming is strongly affected by the SE and SPC, and its constitutive modelling must incorporate the associated micro-scaled mechanisms induced by both factors. This motivates the use of crystal plasticity finite element method (CPFEM) (Asaro and Needleman, 1985; Peirce et al., 1982), for its advantages of involving the grain-level deformation mechanisms (Roters et al., 2010; Tasan et al., 2014). CPFEM simulation with representative volume element (RVE) has been widely used to reproduce mechanical responses and critical microstructures’ evolution (Shang et al., 2020). Based on the phenomenological flow rule and dislocation-density-hardening law, Zhang et al. (2022a) simulated the tensile deformation of Inconel 718 sheets and obtained the relationship between fracture strain and size factor. Tang et al. (2019) established a hardening law based on the Hall-Petch relation to describe the grain-size-dependent initial slip resistance of crystals, thereby the flow stress evolution of sheet metals with different lattice structures was well predicted. To model the twinning in thin TWIP steel sheets, Guo et al. (2020) improved the twin-fraction-based crystal plasticity (CP) model (Sun et al., 2016) via a new size-factor-dependent saturated slip resistance expression, so the erring in micro-scaled deep drawing was well prescribed. CPFEM was also utilized to simulate complex deformation procedures affected by SPC. Based on CPFEM simulation, Hama et al. (2021) found that the evolution of strain rate and stress ratio deviated from each other upon changing strain path. Frodal et al. (2019) used CPFEM simulation to study the plastic anisotropy of aluminum alloys in reversal loading, and the computed yield surfaces well reflected the asymmetry in compression-tension deformation. In the SPC compression of titanium plate, Wronski et al. (2022) elucidated the twinning and de-twinning affected by strain paths through the simulation using visco-plastic self-consistent CP model.

According to the literature review, SE and SPC have been separately studied in corresponding scenarios, but how they cooperatively influence the deformation behavior and microstructure evolution is still unveiled, especially for the micro-scaled

multi-stage deformation. Moreover, the state-of-the-art phenomenological models describing SE and SPC are almost focused on predicting macro-scaled mechanical responses, but the inherent physical mechanisms induced by SE and SPC have not yet been systematically delineated and incorporated in constitutive modelling. Since the grain-level microstructure determines grain's deformation properties, it becomes a must to consider the granular microstructure evolution affected by SE and SPC in constitutive modelling. In our previous work, we performed studies on the mechanical behaviors (Zhang et al., 2021b) and in-grain microstructure evolution (Zhang et al., 2022b) affected by SE and SPC. This study was focused on delineating the intrinsic hardening and softening mechanisms, and establishing an enhanced CP constitutive model involving the influences of SE, SPC, and intragranularly misoriented grain boundaries (IMGBs) (Zhang et al., 2022b) to simulate the micro-scaled SPC deformation of polycrystalline aggregates. Quantitative estimation of the IMGB pattern and magnitude was integrated in CPFEM simulation. Two-stage tensile tests using the ultra-thin (0.1 mm) SS 316L ultra-thin sheets were carried out to systematically explore the influences of SE and SPC. The proposed simulation procedure and constitutive model were validated by the comparative analysis on the stress-strain relationship and microstructure characteristics' evolution. This work advances the understanding and modelling of the SE-affected SPC deformation. It also provides reliable fundamentals of mechanical responses and microstructure evolution, which relieves the experimental cost while designing the multi-stage microforming of ultra-thin sheets.

2. Material preparation and experimental methodology

The annealed commercial austenite SS 316L ultra-thin fine grain (FG) sheet with the thickness of 100.0±2.6 μm was used in this study. The material was subjected to heat treatment in Argon atmosphere, so the sheets with medium and coarse grains (MG and CG) were obtained. Owing to the extreme thinness, the optical microscopy (OM) was performed in the rolling-normal-direction (RD-ND) section. After mirror-like polishing and the chemical etching in aqua regia for about 160 seconds, the mean grain diameters of the samples were measured to be 8.7±0.6, 17.0±2.1 and 31.9±5.7 μm via the linear intercept method given in ASTM E112 standard, as shown in Fig. 1 (a).

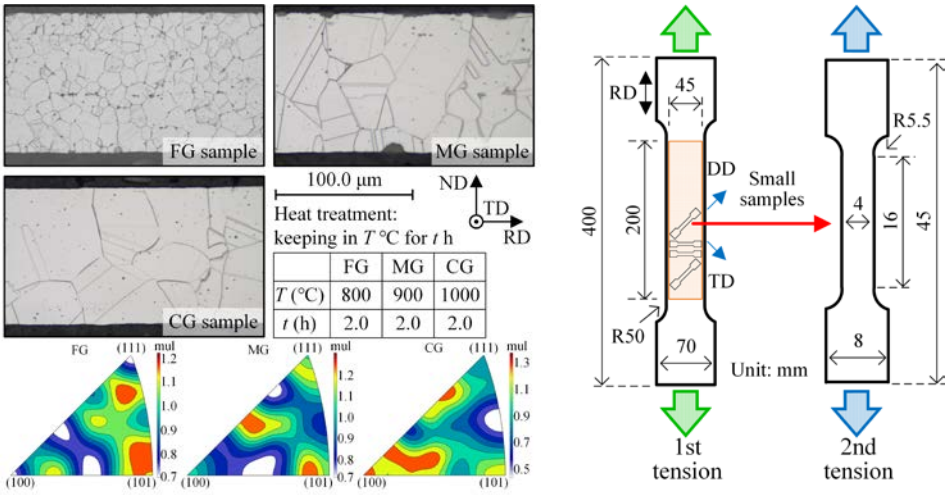

(a) (b)

Fig. 1 Sample preparation and design for the two-stage tensile tests: a) OM metallography, heat treatment conditions, and initial inverse polar figures with a reference direction norm to RD-ND section (unit: multiple uniform distribution abbr. mud), and b) sample dimensions and test schematic.

The two-stage tensile test (Zhang et al., 2021b) and sample dimensions are illustrated in Fig. 1 (b). The larger samples were stretched along RD for pre-strain (ε_{pre}) of 0.06, 0.11 and 0.16 in the first stage, after which the smaller samples were cut along the diagonal direction (DD) and TD for the subsequent tension. In RD-TD plane, the SPC intersection angles (θ_{SPC}) between previous and subsequent loading directions are 45° and 90°, respectively. Since SS 316L is not sensitive to strain rate at room temperature (Renault-Laborne et al., 2018; Samuel et al., 2002), all tests were performed at a tensile speed of 1.0 mm·min^{-1} (a quasi-static state) using the Instron5966 testing machine. Sample surfaces were firstly painted in white and then spread with black speckles, so the strain distribution can be measured via digital image correlation (DIC) using GOM Aramis 4 M optical strain measurement system at a frame rate of 5.0 Hz. Each mechanical test case was repeated for more than three times and the averaged stress-strain data was used for analysis. Electron backscattered diffraction (EBSD) was employed to characterize crystallographic orientation in the polished sections by using NOVA NanoSEM 23 at an acceleration voltage of 20.0 kV with a step size of 0.9 μm. At least three samples for each case were subjected to EBSD characterization, and the measurement magnification was adjusted to ensure that more than twenty grains were detected in each sample section (Zhang et al., 2022b). All the inverse pole figures (IPFs) obtained in EBSD characterization and CPFEM simulation were constructed with a reference direction norm to samples' RD-ND section. Through the extensive characterizations in sample surfaces, representative characteristics of in-grain

microstructures can be obtained and used for analyzing micro-scaled deformation mechanisms.

3. Constitutive modelling framework

Constitutive modelling of the micro-scaled SPC deformation within the CP framework is delineated in this section. Firstly, micro-scaled deformation mechanisms (Zhang et al., 2021b, 2022b) of the main factors, namely SE, SPC and IMGB, would be briefly introduced for an overview of the proposed model. The quantitative estimation (QE) of the IMGB pattern and magnitude, a prerequisite of the model, is established in Section 3.2 based on previous study (Zhang et al., 2022b). Detailed development of the model is described in Section 3.3 and 3.4, and CPFEM simulation setup and procedure are articulated in Section 3.5.

3.1 Micro-scaled mechanisms affected by the main factors

Schematic of the main mechanisms is presented in Fig. 2. In micro scale, the slip of close-packed crystallographic planes accommodates the main plastic deformation of the grains with face-centered cubic (FCC) lattice, so the in-grain microstructures that comprehensively affect the activation and glide of slip planes must be considered in the grain-level constitutive modelling. The IMGBs are consecutive boundaries with nonnegligible misorientations (Zhang et al., 2022b). They impede the movement of dislocations in slip planes and hence raise the deformation resistance of crystals. This hardening effect is governed by several factors such as the pattern and magnitude of IMGB, the spatial relationship and the interaction intensity between IMGB and slip planes. The IMGB-induced hardening can thus be modeled by incorporating the aforementioned factors in constitutive relations, which is delineated in Section 3.4.1.

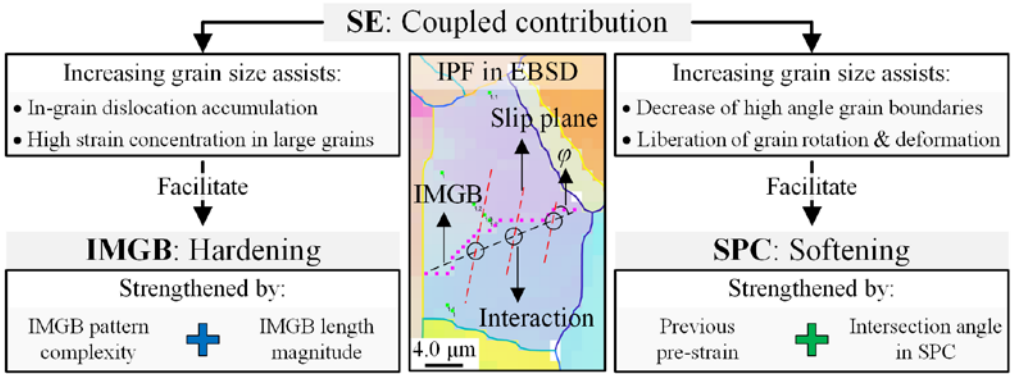

Fig. 2 Schematic of the fundamental mechanisms of IMGB, SPC and SE for modelling the micro-scaled SPC deformation.

According to previous literature reports (Zhang et al., 2021b), subsequent yield

stress of SS 316L ultra-thin sheets is decreased by changing the loading direction. Based on the EBSD characterization, the fraction of grains with relatively high Schmid factors (SFs) are increased in SPC deformation (Parkin and Birosca, 2021; Wu et al., 2020) because of altering loading direction. In addition, grain boundaries are decreased by sample coarsening, so the constraints on grain rotation and deformation are correspondingly loosed. The increase of high SF grains and decrease of grain boundaries both reduce the deformation resistance of ultra-thin sheet. The softening effect induced by SPC would be modelled via describing both two mechanisms in constitutive relations, which is articulated in Section 3.4.2.

Through the sample coarsening, contiguous constraints induced by grain boundaries can be decreased (Li et al., 2019), and the fraction of less-constrained grains in surface layer is improved, so increasing grain size facilitates material softening. On the other hand, the moving path of dislocations before reaching grain boundaries for annihilation is naturally longer in larger grains (Zhang et al., 2020b). This raises the possibilities of dislocation accumulation and tangle, and hence facilitates the formation of intragranular boundaries (Chen and Yu, 2019). In addition to that, larger grains preferentially exhibit higher local strain (Li et al., 2022b) that enhances the accumulation of in-grain misorientations (Harte et al., 2020; Hémery and Villechaise, 2019). Therefore, increasing grain size also improves grains' deformation resistance. Modelling the micro-scaled mechanisms of SE is based on the coupled facilitations to both softening and hardening, which is demonstrated in Section 3.1.3.

3.2 Quantitative estimation of the pattern and magnitude of IMGB

According to previous study (Zhang et al., 2022b), severe incompatible deformation near grain boundary triple junctions (TJ) results in concentrated high strain, leading to the rearrangement of local orientation and hence the formation of IMGB. So IMGB generation is dependent on the local constraints that govern the deformation uniformity near TJs. Moreover, experiments validate that the specific pattern and magnitude of IMGBs are determined by the strain and grain size. For a grain of interest (GOI), the methodology for quantitatively estimating its IMGB is illustrated in Fig. A1 and delineated in this section.

3.2.1 Examination on the geometrical and deformation-related factors

As shown in Fig. A1 (a) and (b), all local constraints, namely the geometrical factors (GeFs) and deformation-related factors (DeFs), will be examined to determine whether the GOI exhibits qualified TJ for IMGB formation. GeFs include the grain boundaries' lengths ($L_1 > L_2$), the inside (θ_{In}) and outside angles ($\theta_{Out1} > \theta_{Out2}$), and they are examined by:

$$\begin{cases} L_2 > 0.1 \cdot P_{GOI} \\ \theta_x \in \left[\theta_{Low\_x}, \theta_{Up\_x} \right], \quad x = In, Out1, Out2 \end{cases} \tag{1}$$

where P_{GOI} is the GOI's perimeter, θ_{Low_x} and θ_{Up_x} are the functions governing the lower and upper bounds of θ_{In} and θ_{Out}, respectively. As shown in Fig. A2 (a-c), the bounds of θ_{Out} and θ_{In} are linearly related to the mean grain diameter ($\bar{d}$),so θ_{Low_x} and θ_{Up_x} can be approximated as:

$$\begin{cases} \theta_{Low\_x}\left(\bar{d}\right) = k_{Low\_x} \cdot \bar{d} + b_{Low\_x} \\ \theta_{Up\_x}\left(\bar{d}\right) = k_{Up\_x} \cdot \bar{d} + b_{Up\_x} \end{cases}, \quad x = In, Out1, Out2 \tag{2}$$

where k_{Low_x}, b_{Low_x} and k_{Up_x}, b_{Up_x} are the slopes and intercepts.

As shown in Fig. A1 (a), DeFs consist of the Schmid factors ($SF_1 > SF_2$) of two adjacent grains and the compatibility factors ($CF_1 > CF_2$) of two grain boundaries. Adjacent grains can be regarded as constraints on the GOI, so the higher their SFs, the more squeeze (or tweak) on the GOI. Moreover, if the deformation accommodation capability of one boundary is significantly lower than the other, then the concentration of high local strain will be triggered (Zhang et al., 2022b). Therefore, the screening conditions for DeFs can be expressed as:

$$\begin{cases} \max\left(SF_1, SF_2\right) > 0.4 \\ \left(CF_1 - CF_2\right) / CF_1 > 0.5 \end{cases} \tag{3}$$

3.2.2 Determination of the IMGB pattern based on the grain area

IMGB pattern determination is performed for grains with qualified TJs. As shown in Fig. A1 (b), if A_{GOI} (the area of GOI) falls into gray region, no obvious IMGB is formed. Similarly, the pattern type can be directly determined when A_{GOI} is located in green (individual IMGB) or red (multiple IMGBs) regions. With the confirmed pattern type, the IMGB magnitude (represented by the summarized IMGB length L_{IMGB}) can be computed by using its linear correlation with A_{GOI} in the third step, as illustrated in Fig. A1 (c).

Grains in blue region of Fig. A2 (d) require additional judgement based on the pattern fractions ($F_{Pattern}$) measured in experiments. Exemplarily, the space between 0 and 1 is divided into two intervals according to the $F_{Pattern}$ of individual and multiple

IMGB grains. After randomly giving a number in [0,1], the pattern type can be determined by checking out this number's ascription interval. The area bounds (A_{Bound}) and $F_{Pattern}$ are governed by exponential functions with respect to ε_{pre} and $\bar{d}$ as:

$$\begin{cases} A_{Bound} = c_{A1} \Big/ \left[1 + c_{A2} \cdot \exp\left(-c_{A3} \cdot \bar{d} \right) \right] - f_{\Delta}\left(\bar{d}, \varepsilon_{pre} \right) \\ f_{\Delta}\left(\bar{d}, \varepsilon_{pre} \right) = c_{A4} * \bar{d} \cdot \left(\varepsilon_{pre} / 0.1 - 1 \right) \\ F_{Pattern} = c_{F1} + c_{F2} \cdot \left(c_{F3} \right)^{\bar{d}} \end{cases} \tag{4}$$

where the coefficients (*c*) with different subscripts in Eq. (2) are summarized in Table A1.

3.3 The crystal plasticity constitutive relationship framework

Under the framework of CPFEM, the phenomenological rate-dependent plastic flow rule is used to describe the slip rate ($\dot{\gamma}^{\alpha}$) evolution in the main slip planes. Driven by the resolve shear stress (τ^{α}), $\dot{\gamma}^{\alpha}$ in the α-th slip system can be computed as:

$$\dot{\gamma}^{\alpha} = \dot{\gamma}_0 \cdot \left(\left| \tau^{\alpha} \right| \Big/ g^{\alpha} \right)^{1/m} \operatorname{sgn}\left(\tau^{\alpha} \right) \tag{5}$$

where g^{α} is the slip resistance, $\dot{\gamma}_0$ and *m* are constants representing the reference slip rate and strain rate sensitivity coefficient, respectively. The deformation gradient tensor ($\mathbf{F}$) of a deformed crystal is composed of:

$$\mathbf{F} = \mathbf{F}^{*}\mathbf{F}^{p} \tag{6}$$

where $\mathbf{F}^{*}$ and $\mathbf{F}^{p}$ are the elastic and plastic part of $\mathbf{F}$. Using the finite strain assumption, the strain measure is:

$$\mathbf{E}^{e} = \left(\mathbf{F}^{*\mathrm{T}}\mathbf{F}^{*} - \mathbf{I} \right) \Big/ 2 \tag{7}$$

where $\mathbf{E}^{e}$ is the Green strain tensor, $\mathbf{I}$ is the identity tensor. Considering about the work conjugation with respect to $\mathbf{E}^{e}$, the 2nd Piola-Kirchhoff stress tensor ($\tilde{\mathbf{T}}$) is thus used as the stress measure, and $\tilde{\mathbf{T}}$ can be computed following the Hooke's law as:

$$\tilde{\mathbf{T}} = \mathbb{C} : \mathbf{E}^{e} \tag{8}$$

where $\mathbb{C}$ is the 4th order elastic tensor. Under the isotropic elastic assumption, it consists three different elements (C_{11}, C_{12}, and C_{44}) in Voigt notation. By using the elastic modulus (E) and Poisson's ratio (υ), they can be computed as:

$$\begin{cases} C_{11} = \dfrac{E(1-\upsilon)}{(1+\upsilon)(1-2\upsilon)} \\ C_{12} = \dfrac{E\upsilon}{(1+\upsilon)(1-2\upsilon)} \\ C_{44} = \dfrac{E}{2(1+\upsilon)} \end{cases} \tag{9}$$

Based on $\tilde{\mathbf{T}}$, τ^{α} can be determined by:

$$\tau^{\alpha} = \left(\mathbf{F}^{*\mathrm{T}}\mathbf{F}^{*} \cdot \tilde{\mathbf{T}}\right) : \mathbf{S}_0^{\alpha} \tag{10}$$

where $\mathbf{S}_0^{\alpha}$ is the Schmid factor tensor (second-order) which is the tensor product of the slip direction unit vector $\mathbf{m}_0^{\alpha}$ and slip plane normal direction unit vector $\mathbf{n}_0^{\alpha}$.

The hardening law describing g^{α} evolution is expressed in a rate form based on its initial (g_0) and saturated slip resistance (g_s) as:

$$\dot{g}^{\alpha} = \sum_{\beta=1}^{12} h_{\alpha\beta} \left|\dot{\gamma}^{\beta}\right| \tag{11}$$

where $h_{\alpha\beta}$ represents the hardening influences of other (e.g. β-th) slip systems on the α-th one, and can be represented by:

$$h_{\alpha\beta} = h_0 \left[q + (1-q)\delta^{\alpha\beta}\right] \left|1 - g^{\beta}/g_s\right|^{n_g} \operatorname{sgn}(1 - g^{\beta}/g_s) \tag{12}$$

where h_0 is the self-hardening coefficient, $\delta^{\alpha\beta}$ is the Kronecker delta, n_g is the slip resistance hardening exponent, q (1.4) represents the strength ratio among different slip systems.

3.4 Establishment of the enhanced CP constitutive relation

3.4.1 IMGB-induced hardening

For the multi-stage microforming, the IMGBs generated in previous deformation cause additional obstruction of crystallographic slip in subsequent deformation. Generally, the IMGB-induced slip resistance is dominated by three aspects: the interaction intensity and the spatial relationship between main slip planes and IMGB, and the stress required for mobile dislocations moving across IMGB.

According to the slip trace studies (Guan et al., 2019; Harte et al., 2020; Sperry et al., 2021), slip systems with the maximum SFs determined under the uniaxial external loading conditions, were activated during plastic deformation. Moreover, it was not practical to characterize the actual stress states (which may deviate from the external loading state to some extends) of grains inside samples via current EBSD, so the assumption that the grains were in uniaxial tensile stress state was employed in this study. In that condition, the maximum resolved shear stress in each main slip plane is then determined by the corresponding highest SF. The main slip planes of FCC crystal are denoted by the subscript "*i*" (1~4). Each slip plane exhibits three SFs according to the slip directions, and the maximum one (SF_{i_Max}) is used to represent the potential activation capability of the i-th slip plane. In general, the greater SF_{i_Max}, the easier dislocation movement, so the interactions between the dislocations (in the i-th slip plane) and IMGB is more intense. In that condition, the impedance of IMGBs on slip is stronger and the IMGB-induced slip resistance is improved. As illustrated in Fig. 3, aforementioned spatial relationship is dependent on IMGB's geometrical complexity that can be represented by a function (f_{Geo}) with respect to L_{IMGB} and the intersection angle ($0 \le \varphi_i \le 90^o$). The IMGB-induced slip resistance (g_{IMGB}^i) can thus be expressed as:

$$g_{IMGB}^i = \left(SF_{i\_Max}/0.5\right) \cdot f_{Geo}^i\left(L_{IMGB}, \varphi_i\right) \cdot s_{Mag} \tag{13}$$

where $(SF_{i\_Max}/0.5)$ represents the SF-dominated interaction intensity, and s_{Mag} represents the stress for incident dislocations moving across IMGB. f_{Geo}^i can be represented by:

$$f_{Geo}^i = \left(L_{IMGB}/\bar{d}\right)^{\kappa} \cdot \sin\varphi_i \tag{14}$$

where κ is defined as the hardening exponent. Normalizing the IMGB magnitude with $\bar{d}$ minimizes the interferences of grain diameter divergence. Since the grains with multiple IMGBs generally exhibit greater L_{IMGB}, the contribution of IMGB pattern complexity is implicitly incorporated in this ratio. For the grains with individual

IMGB, exact φ_i can be easily determined, so φ_i of each main slip plane is distinct in Eq. (14). For the grains with multiple IMGBs, a slip plane will intersect with several IMGBs simultaneously and has several values for its intersection angle, because the IMGBs with different spatial attitudes are spread in the whole grain. In that condition, φ_i would easily reach high among its all-possible values. Moreover, IMGBs are generally longer and exhibit greater misorientation angle in this condition, so multiple IMGBs impose more intense obstructions on all slip planes. Considering about these facts, the maximum (90°) is used as φ_i for all slip planes to represent the much stronger hardening effects in cases with multiple IMGBs. Notably, this processing simplifies the complex intersection states between IMGBs and close-packed planes, but the differences between the spatial attitudes of main slip planes are still preserved, which is represented by different SF_{i_Max} in Eq. (13). Therefore, the IMGB-induced slip resistance for each slip plane is still different from each other in grains with multiple IMGBs.

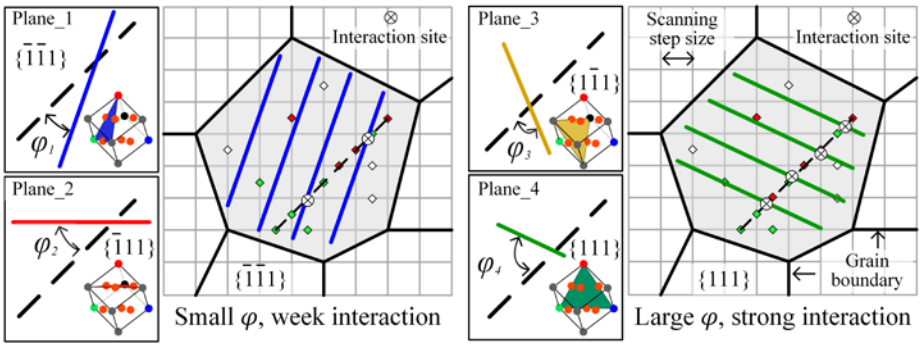

Fig. 3 Illustration of the spatial relationship between main slip planes and IMGB.

The slip of close-packed plane is accomplished by the movement of dislocations. When the dislocations in slip plane move to IMGBs, the propagation of slip requires the dislocations moving across IMGBs. Since IMGBs contain dislocations, they impose obstruction on these incident dislocations. This impedance stress is just the third part of IMGB-induced slip resistance, and is denoted by s_{Mag}. As illustrated in Fig. 4, while the incident dislocation moving across IMGB, it is obstructed by the stress field generated by IMGB dislocations. The higher dislocation density, the stronger obstruction. Based on the Taylor hardening assumption (Ashby, 1970; Taylor, 1934), s_{Mag} can be expressed as:

$$s_{Mag} = M\upsilon Gb\sqrt{\rho_{IMGB}} \tag{15}$$

where M is the average Taylor factor (Mecking and Kocks, 1981), υ is a material constant (Barlat et al., 2002), G is the shear modulus, and b is the magnitude of the Burgers vector (Robertson et al., 2001). Since IMGBs are low angle grain boundaries, the mean spacing ($\overline{l}$) between the dislocations in IMGB can be approximated as:

$$\overline{l} = b/\overline{\theta}_{Mis} \tag{16}$$

where $\overline{\theta}_{Mis}$ (rad) is the mean misorientation angle in IMGB and exhibits different values for the individual and multiple pattern ($\overline{\theta}_{Mis\_Ind}$ and $\overline{\theta}_{Mis\_Mul}$). The dislocation density in IMGB can thus be estimated by:

$$\rho_{IMGB} = \left(L_{IMGB}/\overline{l}\right)/A_{GOI} \tag{17}$$

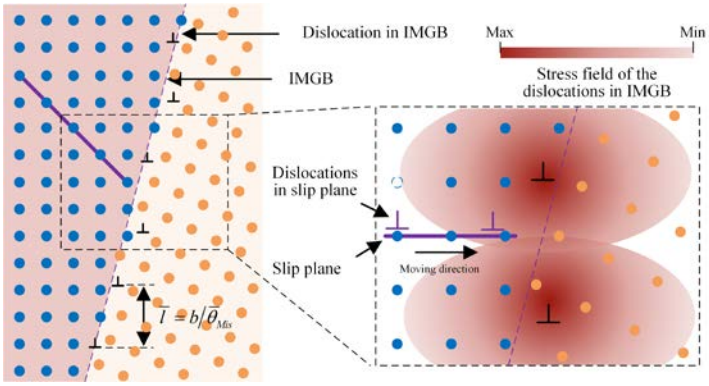

Fig. 4 Illustration of the IMGB obstruction: incident dislocations in slip planes moving across the stress field generated by the dislocations in IMGB.

Substituting Eq.s (16) and (17) into Eq. (15) yields:

$$s_{Mag} = M\upsilon G\sqrt{L_{IMGB}\overline{\theta}_{Mis}b/A_{GOI}} \tag{18}$$

Explicit expression of the IMGB-induced slip resistance can be obtained by using Eq.s (14) and (18), and it is used to improve the hardening rules employed by conventional CPFEM computation.

3.4.2 SPC-induced softening

Subsequent flow stress of 316L austenite steel in SPC tension is lower than that in monotonic tension (Zhang et al., 2021b). Previous deformation drives the grains towards a certain orientation, so loading direction alternation improves the fraction of high SF grains, leading to the reduction of external loading for plastic deformation (Parkin and Birosca, 2021; Wu et al., 2020). The contribution of high SF grain fraction

to material softening can be estimated by ψ (Zhang et al., 2021b) as:

$$\psi = \varepsilon_{pre} \cdot \left(1 - \delta_{SPC}\right)^2 \tag{19}$$

where δ_{SPC} is the SPC parameter (Ha et al., 2013; Schmitt et al., 1985) as defined in Appendix B. The higher ψ implies that more grains are arranged in the "soft orientation", so it's easier to deformed the samples in subsequent loading. Accompanied with Eq. (B4), the SPC-induced decrease of slip resistance (Δg_{SPC}) can be expressed as:

$$\Delta g_{SPC} = \varepsilon_{pre} \cdot f\left(\bar{d}\right) \cdot \xi_{SPC} \cdot \left(0.91 \cdot \theta_{SPC}\right)^{2 \cdot \omega_{SPC}} \tag{20}$$

where $f(\bar{d})$ is the grain-size-dependent function, ω_{SPC} and ξ_{SPC} are the SPC intensity exponent and coefficient that quantify the softening purely induced by SPC.

3.4.3 Coupled facilitation caused by SE

Governed by the Hall-Petch relation, the softening effect of increasing the grain size is involved in the fundamental parameters of CP constitutive model, which would be articulated in Section 4.2.1. For the hardening effect induced by SE, $f(\bar{d})$ quantifies the influences of grain size on Δg_{SPC} as designated in Eq. (20). Moreover, since larger grains generally exhibit more IMGBs with complex pattern (Hémery and Villechaise, 2019; Li et al., 2022b), they generally exhibit greater L_{IMGB}. So increasing grain size contributes to promoting the slip resistance via improving L_{IMGB} as (Zhang et al., 2022b):

$$L_{IMGB} = p_{1\_k} \cdot A_{GOI} + p_{2\_k}, \quad k = Ind, Mul \tag{21}$$

where p_{1_k} (μm^{-1}) and p_{2_k} (μm) are the slope and intercept, and they can be computed by:

$$p_{j\_k} = \chi_{j\_k} \cdot \bar{d}^{\,\omega_{j\_k}}, \qquad j = 1, 2 \tag{22}$$

where χ_{j_k} and ω_{j_k} are fitting parameters based on experimental results.

3.4.4 Integrating the micro-scaled mechanisms in CP framework

Computation of the proposed model is illustrated in Fig. 5. Conventional CP constitutive relationship is enhanced via incorporating the aforementioned micro-scaled mechanisms. As IMGBs permanently remained in the grains after previous deformation, they impede the dislocation movement perpetually in subsequent loading. Therefore, the IMGB-induced hardening effect is incorporated in determining the saturated slip resistance in SPC deformation. For a GOI with IMGBs, its overall g_{IMGB}^{GOI} can be computed by the weighted mean of all four g_{IMGB}^{i} as:

$$g_{IMGB}^{GOI} = \frac{1}{4} \cdot \sum_{i=1}^{4} \left(g_{IMGB}^{i} \cdot SF_{i\_max} \Big/ \sum_{i=1}^{4} SF_{i\_max} \right) \tag{23}$$

The saturated slip resistance in SPC deformation ($g_{s\_SPC}^{GOI}$) can thus be expressed as:

$$g_{s\_SPC}^{GOI} = g_s + g_{IMGB}^{GOI} \tag{24}$$

where g_{IMGB}^{GOI} is calculated by Eq.s (13), (14), (18), and (23).

Since yield stress is mainly dominated by the initial slip resistance in CPFEM (Appendix C), the SPC-induced softening is integrated in the determination of the initial slip resistance (g_{0_SPC}) for SPC deformation. Owning to the work hardening in previous deformation, current slip resistance (g_{pre}) evolves with pre-strain, and g_{0_SPC} is correspondingly expressed as:

$$g_{0\_SPC} = g_{pre} - \Delta g_{SPC} \tag{25}$$

where Δg_{SPC} is computed based on Eq. (20), and g_{pre} is determined following Appendix C.

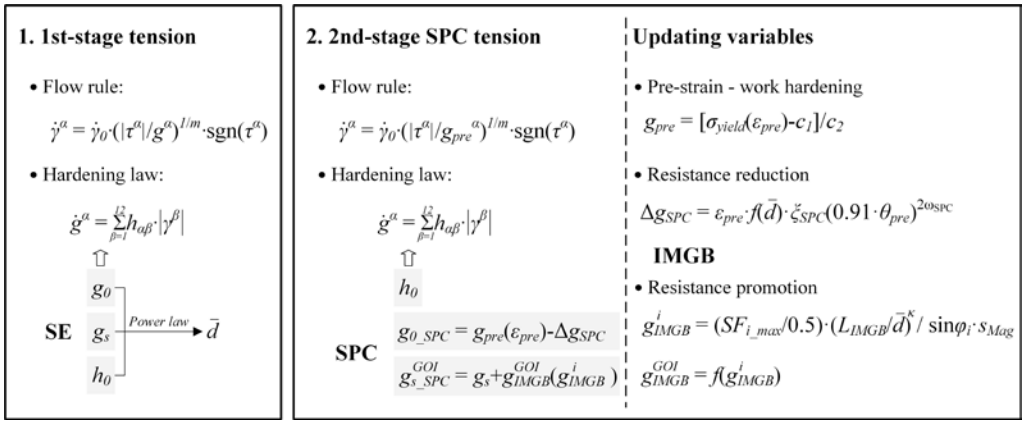

Fig. 5 Computation illustration of the enhanced CP model for simulating the micro-scaled SPC deformation via CPFEM.

3.5 Numerical implementation of the improved constitutive relation

The RVEs are divided into polyhedron cell aggregates via Voronoi tessellation method, as shown in Fig. 6. Cell's mean sizes were set as the same with the mean grain sizes of corresponding samples. Referring to samples' initial IPFs shown in Fig. 1 (a), random Euler angles were assigned to each cell in simulation. The thickness (along Z axis) is fixed as 0.1 mm, and the length and width are adjusted for involving at least six and three grains along RD and TD (X and Y axis), respectively. This dimensional manipulation improves the computation efficiency and also ensures enough grains are deformed. The open-source code kit DAMASK (Roters et al., 2019) is used for CPFEM simulation. RVE is firstly stretched along X for certain pre-strain (0.06, 0.11, and 0.16), and then the stretched along Y for plastic strain till 0.1 in the second stage.

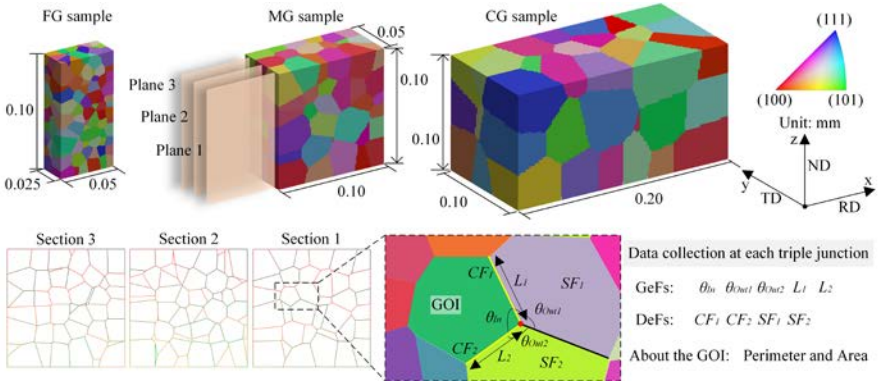

Fig. 6 Illustrations of RVEs and the extraction of local constraint information in RD-ND section.

Fig. 7 illustrates the numerical simulation and analysis procedure. To acquire the GeFs and DeFs of the polycrystalline aggregates, three equidistant planes distributed

along TD are used to intersect with the RVEs, as shown in Fig. 6. These sections are used to extract the local constraint datasets for estimating the IMGB pattern and magnitude. The first stage stress-strain curve is used to identify the relationship between fundamental CPFEM parameters and $\bar{d}$. Inspired by (Sedighiani et al., 2021), a remeshing RVE inheriting the deformed state is built for preventing grid distortion in subsequent deformation. The enhanced constitutive model is used in the second stage simulation, and comparative analysis is carried out for validating the proposed model and simulation scheme.

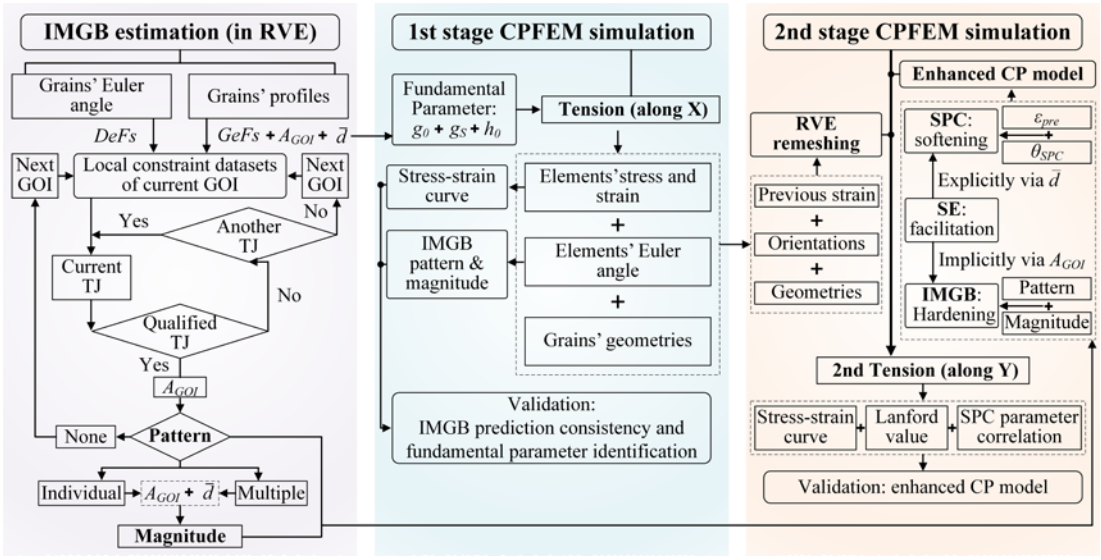

Fig. 7 Flow chart of the CPFEM simulation and analysis procedure using the enhanced CP constitutive model.

4. Experimental and simulation results

4.1 Experimental results

4.1.1 Flow stress

Fig. 8 presents the second stage tensile stress-strain curves that are offset by the corresponding pre-strain (Barlat et al., 2014; Qin et al., 2017). The second stage flow stress is universally lower than monotonic one, and their deviations are increased with ε_{pre} and θ_{SPC}, showing the softening effect induced by SPC. The flow stress of both tensile stages is decreased with the increase of grain size, which is consistent with the Hall-Petch relationship.

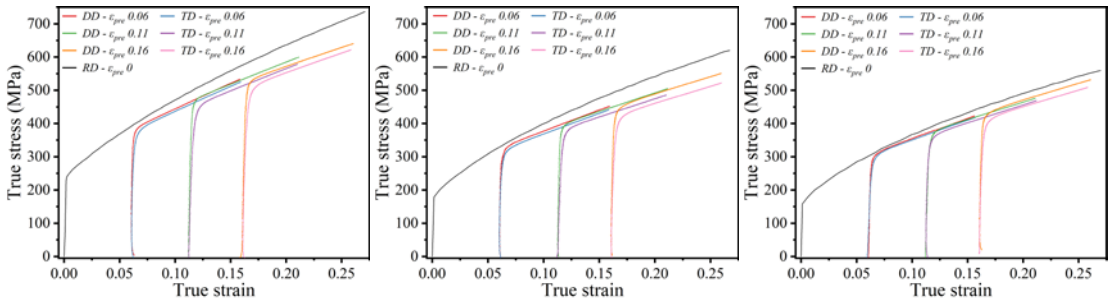

Fig. 8 True stress-strain curves in the second stage tensile tests along DD and TD: results of a) FG, b) MG, and c) CG samples.

The reduction of subsequent yield stress is shown in Fig. 9 (a). For FG samples, when ε_{pre} is increased from 0.06 to 0.11, the reduction is promoted from 25.3 to 46.9 MPa along DD, and got increased from 37.2 to 68.7 MPa along TD. For MG samples with pre-strain of 0.11, the reduction is improved from 44.2 to 65.9 MPa while θ_{SPC} is increased from 45 to 90°. These suggest that the yield stress reduction can be enhanced by increasing ε_{pre} and θ_{SPC}. It is worth noting that this reduction is decreased after increasing grain size. For example, with pre-strain of 0.16, the reductions are 68.5 and 101.1 MPa along DD and TD in FG samples, but they are minimized to 40.8 and 59.8 MPa in CG samples. Fig. 9 (b) shows the strain hardening rate (λ) defined as ($\mathrm{d}\sigma/\mathrm{d}\varepsilon$) where σ and ε are true stress and strain, respectively. The hardening rates along DD and TD are similar, demonstrating that λ is insensitive to θ_{SPC}. λ is decreased by increasing ε_{pre} and $\bar{d}$, but the later one's impacts gradually vanished, as the hardening rates of MG and CG samples have already become similar.

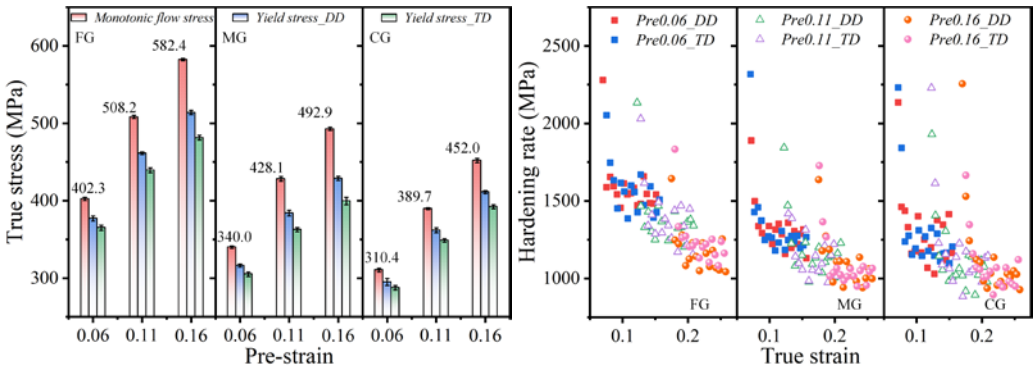

Fig. 9 Main mechanical properties' variation induced by SE and SPC: a) the second stage yield stress and monotonic tensile flow stress at the same pre-strain, and b) the strain hardening rates in the second stage tensile tests.

4.1.2 Lankford coefficient

The Lankford coefficient (r-value) is an important parameter used in SPC-related modelling. Fig. 10 presents the major and minor strain measured via DIC, and the mean Lankford coefficients obtained in the second stage tensile tests along DD and TD (r_{DD} and r_{TD}) are listed in Table 1. r-value increases with ε_{pre}, implying that the deformation resistance in thickness direction is improved by previous deformation. Under the same conditions, r_{DD} is universally greater than r_{TD}, which is consistent with other observations in low carbon steel (Ha et al., 2013; Zaman et al., 2018). Increasing grain size not only results in the decrease of Lankford coefficient, but also diminishes the variations induced by increasing ε_{pre} and θ_{SPC}. This suggests that the deformation-induced anisotropy can be reduced in coarse-grained samples.

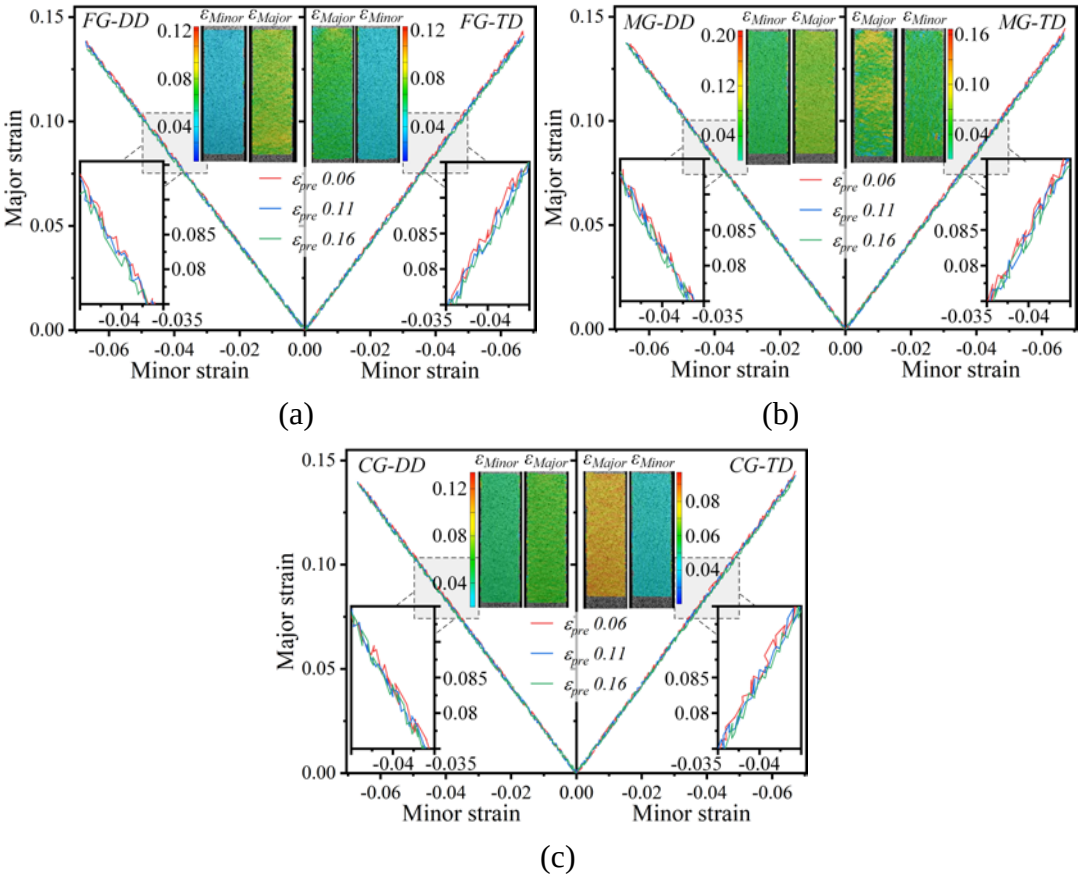

Fig. 10 The major and minor strain in the second stage tensile tests along DD and TD: results of a) FG, b) MG, and c) CG samples.

Table 1 Lankford coefficients obtained in the second stage tensile tests (r_{DD}, r_{TD})

Grain size	ε_{pre} 0.06	ε_{pre} 0.11	ε_{pre} 0.16

FG	(0.941, 0.881)	(0.956, 0.895)	(0.967, 0.911)
MG	(0.932, 0.875)	(0.942, 0.889)	(0.951, 0.899)
CG	(0.913, 0.871)	(0.927, 0.883)	(0.938, 0.891)

4.1.3 Fraction of high SF grains

Based on the Euler angles measured by EBSD, the maximum SF of main slip systems $(111)[1\bar{1}0]$ can be computed and used to determine the fractions (ϕ) of grains with SF greater than 0.4. As presented in Fig. 11 (a), ϕ is decreased with the increase of ε_{pre}, meaning that overall SFs are decreased after straining. This is attributed to the fact that the norm of slip plane gradually approaches to the stretching direction, leading to the decrease of SF. Moreover, the decrease of ϕ in CG samples is more sensitive to strain, because undeformed coarse-grained samples exhibit the highest ϕ while this fraction becomes the lowest after ε_{pre} reaches 0.16. As shown in Fig. 11 (b), ϕ is immediately increased upon changing the loading direction. More straining drives grains toward hard orientations that turns out to be soft ones after increasing θ_{SPC}, so the increase of ε_{pre} and θ_{SPC} assists the SF promotion and hence increases ϕ at the beginning of SPC tension. This is the grain-level softening mechanism induced by SPC. Grains becomes easier to be rotated after loosening their constraints via increasing grain size, the variation of ϕ is thus more significant in coarse-grained samples. Therefore, the SPC-induced softening can be enhanced by increasing ε_{pre}, θ_{SPC}, and $\bar{d}$.

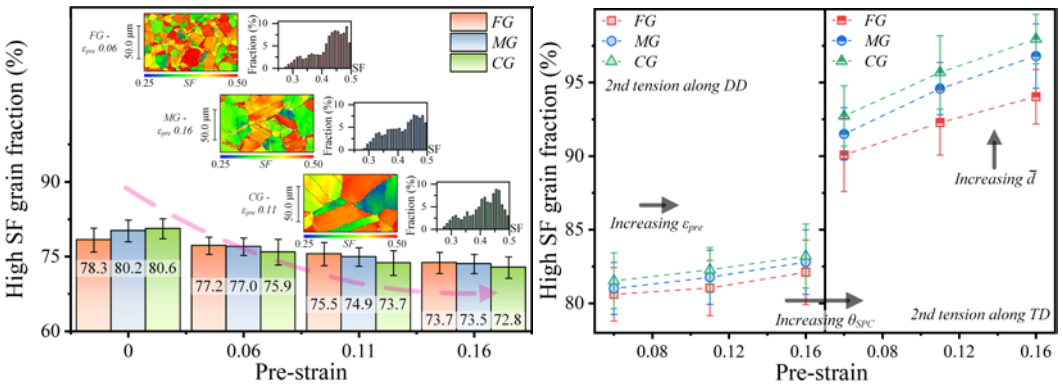

(a) (b)

Fig. 11 Evolution of the high SF grain fractions: a) the results obtained after the first stage uniaxial tension, and b) the results collected at the beginning of the second stage SPC tension.

4.2 Parameter identification method

4.2.1 Determination of fundamental parameters

True stress-strain curves of the first stage tension are plotted in Fig. 12 (a). The mean elastic modulus (180 GPa, as shown in Fig. 12 a) and Poisson's ratio of 1/3 were used to compute C_{11}, C_{12}, and C_{44} following Eq. (9). The material constants used in the simulation, namely $\dot{\gamma}_0$, m, and n_g are listed in Table 2. The fundamental CPFEM parameters are determined by repeating the simulation with different inputs until the predicted flow stress curves exhibit good fits (deviation below 5.0%) with experimental ones (Tang et al., 2019). As presented in Table 2, the identified initial and saturated slip resistance are decreased with the increase of grain size, so with the self-hardening coefficient. Although grain orientations are uniform before deformation, but a preference of (101) is observed after deformation, as exemplarily shown in Fig. 13(a). Fig. 13(b) presents the concentrations of representative orientations, the intensity near (101) is increased with strain and grain size, which is consistent with the experimental observations (Zhang et al., 2021b).

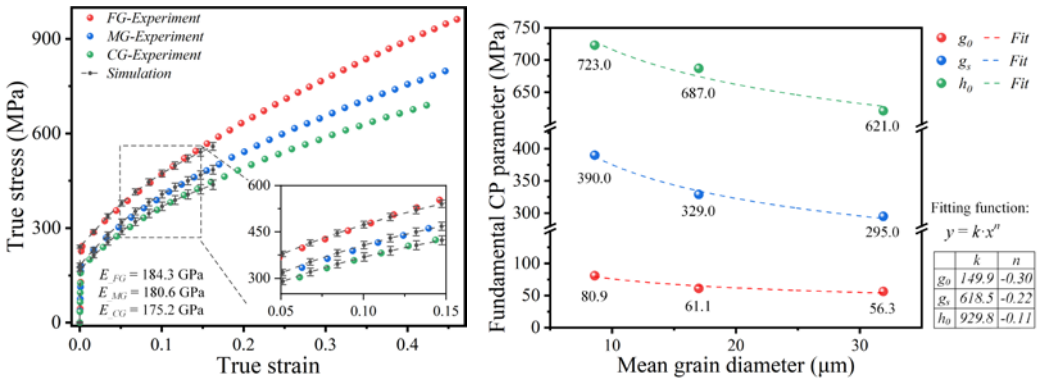

(a) (b)

Fig. 12 Determination of fundamental parameters for CPFEM simulation: a) best fit of the experimental stress-strain curve, and b) power law relationship between parameters and mean grain size.

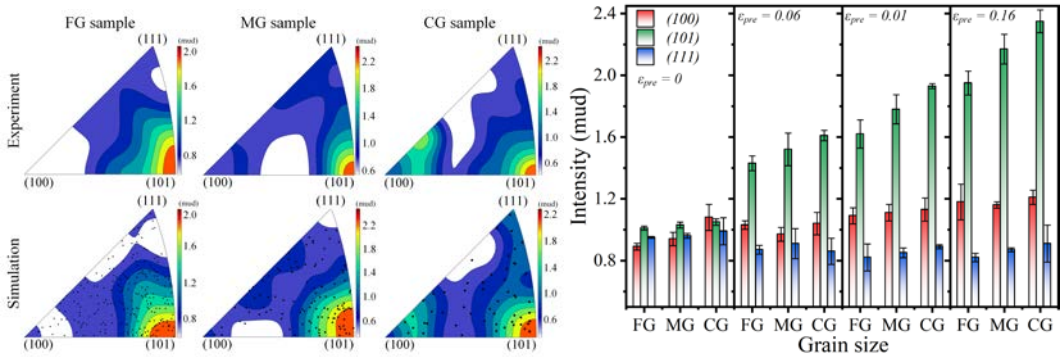

(a) (b)

Fig. 13 Deformation-induced orientation concentration: a) contouring mapping of grain orientation distribution (with a reference direction norm to samples' RD-ND section) at the pre-strain of 0.16, and b) samples' orientation intensity in different deformation conditions.

Table 2 Fundamental CPFEM parameters of SS 316L ultra-thin sheets with different mean grain sizes. (The units of C_{11}, C_{12}, and C_{44} are GPa. The units of g_0, g_s, and h_0 are MPa)

Grain size	C_{11}	C_{12}	C_{44}	$\dot{\gamma}_0$	m	n_g	g_0	g_s	h_0
FG							80.9	390.0	723.0
MG	270.0	135.0	67.5	0.0001	0.1	2.5	61.1	329.0	687.0
CG							56.3	295.0	621.0

The fundamental parameters, namely g_0, g_s and h_0, generally exhibit different values when sample grain size is changed. Their results listed in Table 2 are plotted with respect to $\bar{d}$ in Fig. 12(b). The presented correlation is well fitted by exponent function, which agrees with the principles of Hall-Petch relationship. This implies that the primary SE-induced softening has been implicitly involved in these parameters. The presented grain-size-dependent correlation provides references of these parameters, which releases the cost of trial-and-error attempts in parameter identification.

4.2.2 Determination of advanced parameters

In SPC deformation condition, determination of the advanced parameters consists of the IMGB-induced hardening part (g_{IMGB}^{GOI}) and the SPC-induced softening part (Δg_{SPC}). In terms of the former one, the coefficients and constants needed in Eq. (14) and (18) are summarized in Table 3. The hardening exponent κ takes 0.5, and $\bar{\theta}_{Mis}$ takes 1.5° and 3.0° for individual and multiple IMGBs, respectively (Zhang et al., 2022b). The other constants are obtained in (Barlat et al., 2002; Robertson et al., 2001). L_{IMGB} is computed by Eq. (21) where the slope and intercept are determined by Eq. (22) based on χ_{j_k} and ω_{j_k} (Zhang et al., 2022b) given in Table 3. With the determined IMGB pattern and A_{GOI}, g_{IMGB}^{i} of each main slip plane can be computed by Eq. (13) and then used for calculating g_{IMGB}^{GOI} using Eq. (23).

Table 3 The coefficients and constants used in the improved constitutive relation.

Eq. (14), (18)		Eq. (18)		Eq. (22)		
				χ_{j_k}	ω_{j_k}	
κ	0.5	M	3.0	p_{1_Ind}	1.195	-0.9112
$\bar{\theta}_{Mis\_Ind}$	0.026	υ	0.33	p_{2_Ind}	0.1378	0.9539
$\bar{\theta}_{Mis\_Mul}$	0.052	G	67500.0	p_{1_Mul}	6.164	-1.245
		b	$2.54\text{x}10^{-4}$	p_{2_Mul}	1.075	0.7273

For the SPC-induced softening part, g_{pre} and Δg_{SPC} must be determined to compute g_{0_SPC} according to Eq. (25). According to Appendix C, the yield stress given by CPFEM simulation is mainly governed by initial slip resistance. Previous "loading and reloading" monotonic tensile tests (Zhang et al., 2020a) prove that the "reloading" yield stress is approximately equal to the monotonic flow stress at the same strain. Therefore, the evolved slip resistance g_{pre} can be treated as the "updated" initial slip resistance while reloading, and it can be obtained by substituting the left side of Eq. (C2) with the monotonic tensile flow stress at corresponding pre-strain. Similarly, the yield stress of SPC tension along DD is used to replace the left side of Eq. (C2) for computing g_{0_SPC}.

By using Eq. (25), Δg_{SPC} can be calculated based on g_{pre} and g_{0_SPC}. To quantitatively distinguish the contribution of ε_{pre} and θ_{SPC}, the equivalent slip resistance decrease (Δg^{*}_{SPC}) is defined as the ratio between Δg_{SPC} and ε_{pre}. As shown in the enlarged window of Fig. 14 (a), variation of pre-strain scarcely changes Δg^{*}_{SPC}, suggesting that Δg^{*}_{SPC} is purely governed by $\bar{d}$ and θ_{SPC}. This also validates that incorporating ε_{pre} as a multiplier in Eq. (20) is reasonable to describe the contribution of pre-strain. By giving the best fit of Δg^{*}_{SPC} (dash line), ω_{SPC}, ξ_{SPC} and $f(\bar{d})$ can be determined:

$$\begin{cases} \omega_{SPC} = 0.278,\ \xi_{SPC} = 1.205 \\ f\left(\bar{d}\right) = 170.461 - 1.823 * \exp\left(\bar{d}/\bar{d}_0\right) \end{cases} \tag{26}$$

where $\bar{d}_0$ (8.7 μm) is the minimum mean grain size of the used samples, $f(\bar{d})$ is an exponential decay function and is negatively related to $\bar{d}$. $f(\bar{d})$ is decreased with the increase of $\bar{d}$, resulting in fewer yield stress reduction in SPC deformation, which

is consistent with the experimental observations.

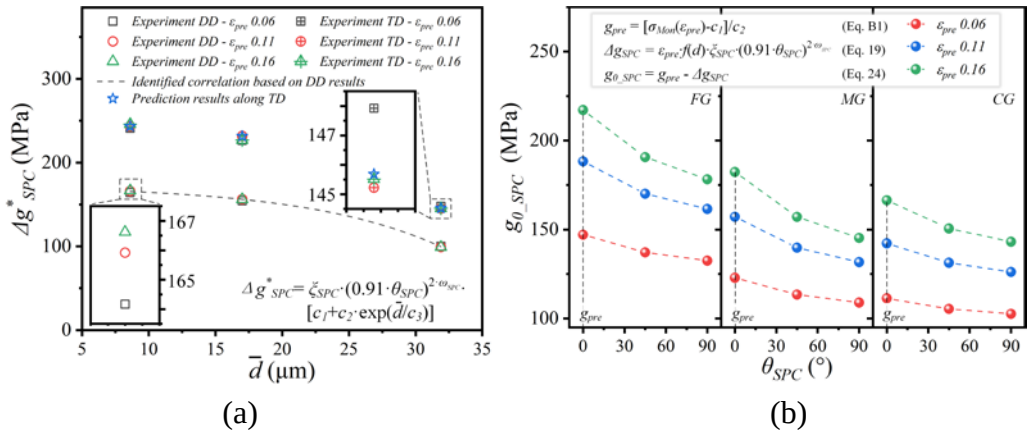

Fig. 14 The parameter identification of SPC-induced softening part: a) the equivalent slip resistance decrease, and b) the computed g_{0_SPC} indifferent conditions.

The experimental Δg^*_{SPC} along TD is used for validation. Predictions of Δg^*_{SPC} in TD are computed by Eq. (20) and (26), and denoted as stars in Fig. 14 (a). Both results show good consistency, suggesting that the identified parameters are reliable to describe the slip resistance reduction induced by SPC. The g_{0_SPC} of all experimental cases are summarized in Fig. 14 (b). Increasing θ_{SPC} leads to the decrease of g_{0_SPC}, and this tendency is enhanced when ε_{pre} is raised. g_{0_SPC} is universally decreased with the increase of grain size, and this arises from the smaller g_{pre} in coarse-grained samples. Due to the exponential decay function $f(\bar{d})$, the reduction of g_{0_SPC} caused by increasing θ_{SPC} is also minimized after increasing $\bar{d}$, and this also agrees with experimental results.

4.3 Simulation results and validation

4.3.1 Prediction of the flow stress in micro-scaled SPC deformation

Both the conventional CP model and the proposed model are used to simulate the deformation of RVEs with different ε_{pre} and $\bar{d}$ in the second stage tension along TD. As shown in Fig. 15, conventional model overestimated the yield stress and hardening rate obviously, and the deviations are dramatically increased with ε_{pre} and $\bar{d}$. Compared with that, the softening effects induced by SPC and grain coarsening are incorporated in the proposed model, so its stress-strain curves are shifted down and agree well with experimental results.

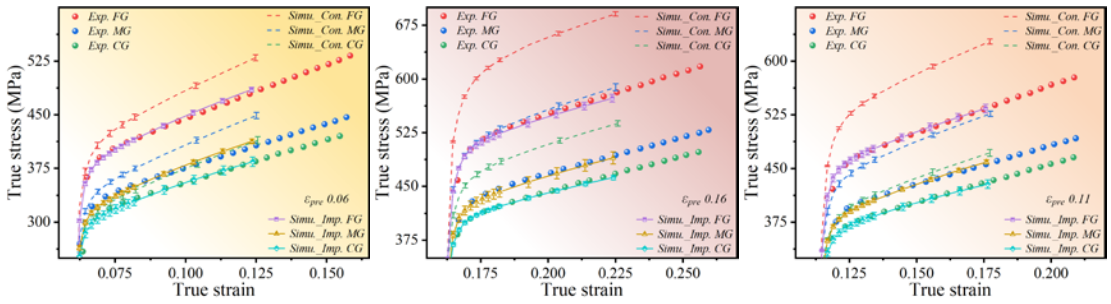

Fig. 15 The performance of conventional and improved CP constitutive model in predicting the second stage tensile flow stress with pre-strain of : a) 0.06, b) 0.11, and c) 0.16. Exp. denotes experimental results, and Simu._Con. and Simu_Imp. denotes the simulation using conventional and proposed model, respectively.

Notably, the deviation of yield stress is also slightly increased with ε_{pre} and $\bar{d}$ though the proposed model is used, implying that the modelling of SPC deformation still awaits improvements. Current description of the softening mechanisms induced by high SF grain fraction is in half-empirical manners. Although they are integrated in the proposed model, but deeper explorations such as the analysis on dislocation dynamics and recrystallization (Li et al., 2022a; Sun et al., 2022), are required for a step forward investigation. Despite of the deviations, the proposed model still provides good prediction about the flow stress in micro-scaled SPC deformation. It incorporates more inherent micro-scaled deformation mechanisms than conventional CP model and other macro-scaled model (Zhang et al., 2021b), which enables higher flexibility and accuracy of the proposed model.

4.3.2 Prediction of the evolution of microstructure characteristics

Performance of predicting the microstructure characteristics' evolution is also evaluated. Fig. 16 shows the Lankford coefficients obtained in experiments and simulation. Although both models underestimate the r-value, predictions given by the proposed model are still much closer to experimental results. IMGB pattern and magnitude are involved in the proposed model to describe distinct obstructions for each slip plane. Thereby, each grain's deformation-induced anisotropy is considered during simulation, resulting in better prediction of r-value.

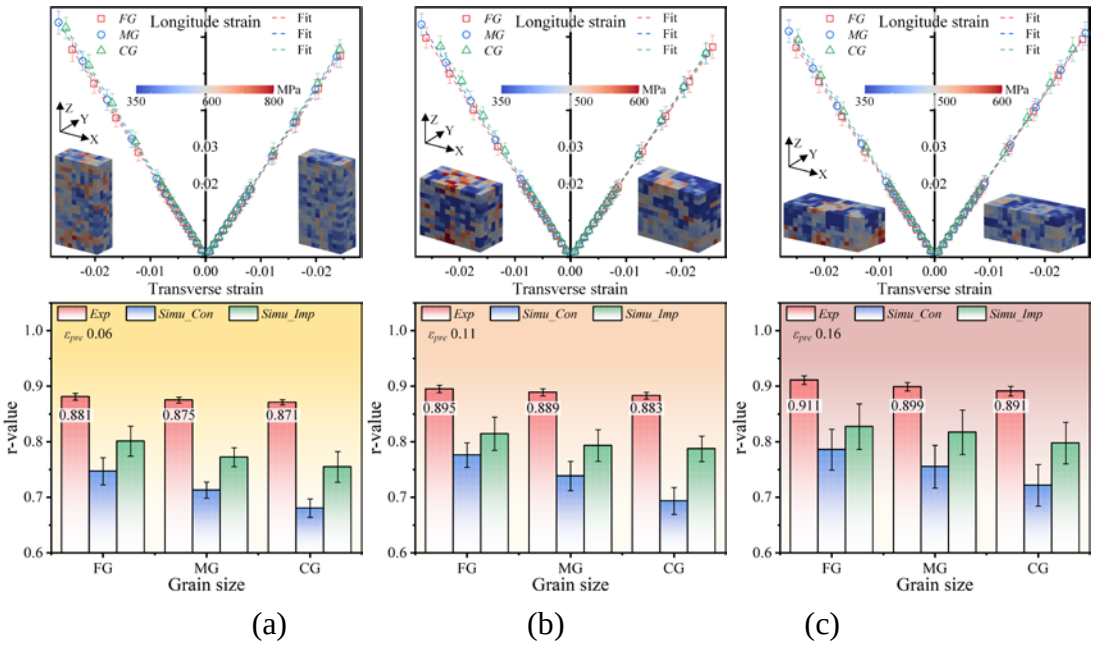

(a) (b) (c)

Fig. 16 Evaluation of predicting Lankford value: strain correlation and r-value with pre-strain of a) 0.06, b) 0.11, and c) 0.16. In the second stage tension along TD, longitude strain aligns with Y and transverse strain aligns with X.

The SPC parameters are compared in Fig. 17 (a). The maximum deviation of δ_{SPC} is about 0.035, and the relative underestimation is below 10.0%. The predicted $(1-\delta_{SPC})^2$ are also quite close to experimental results with ultimate deviation about 5.1%. This suggests that current simulation still provides reliable estimations of these important SPC-related characteristics. The correlation between high SF grain fraction and $(1-\delta_{SPC})$ is shown in Fig. 17 (b) where the predicted ϕ and $(1-\delta_{SPC})$ fit with the relationship acquired in experiments. This manifests that it is rational to use the parabola expression (Eq. 18) to quantify the influences of high SF grain fraction on SPC deformation, and the proposed constitutive model is adequate to predict the evolution of critical microstructure characteristics.

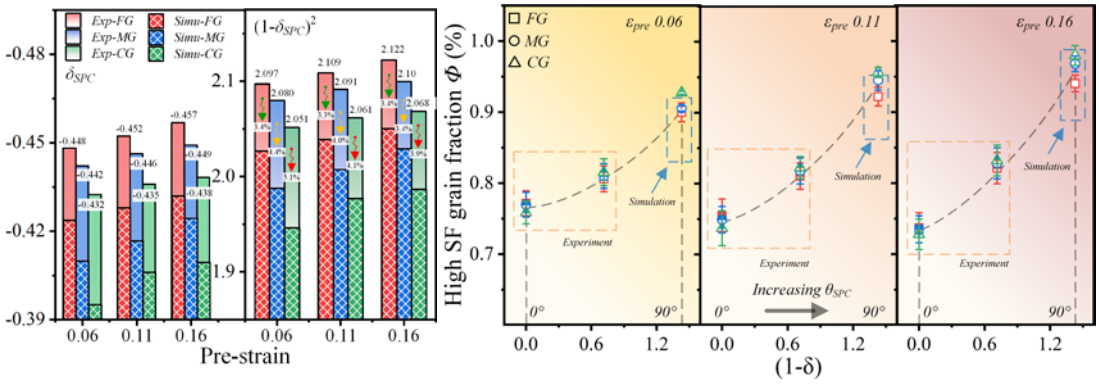

(a) (b)

Fig. 17 Evaluation of predicting the SPC-parameter and its correlation with high SF grain fraction: a) prediction of the SPC-parameter, and b) consistency comparison between the experimental and simulation results about the parabola relationship.

5. Discussion and analysis

5.1 Evaluation of the QE method

The proposed CP model needs the information of IMGB pattern and magnitude which, however, are provided by the QE method rather than CPFEM simulation itself, so it is necessary to examine the consistency between the results given by QE (QE results) and CPFEM simulation (CP results). Following (Zhang et al., 2022b), IMGBs can be extracted from the IPFs provided in simulation, and comparison between both results are exemplarily shown in Fig. 18. Clear IMGBs are recognized in the IPFs of CP results, and they exhibit similar configuration to the EBSD characterization results (Zhang et al., 2022b). Most of the qualified TJs predicted by QE (denoted by stars in) are consistent with CP results, though some sites of CP results are missed by QE. For the determination of IMGB information, only the existence of qualified TJs is concerned in the examination herein. In other words, the deviation about their locations and quantities would not deteriorate the follow-up estimation of IMGB pattern and magnitude.

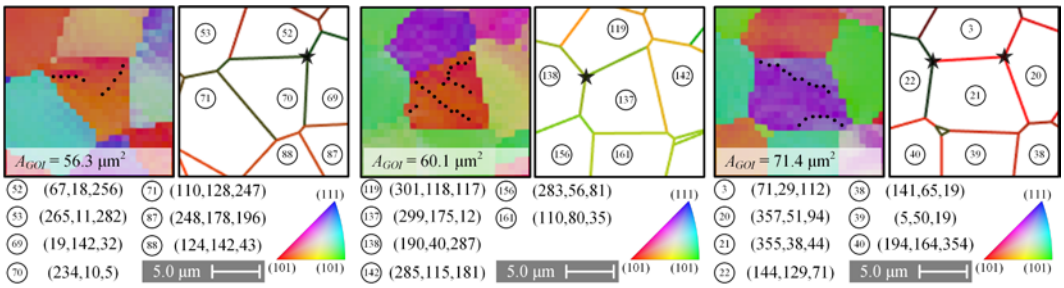

(a)

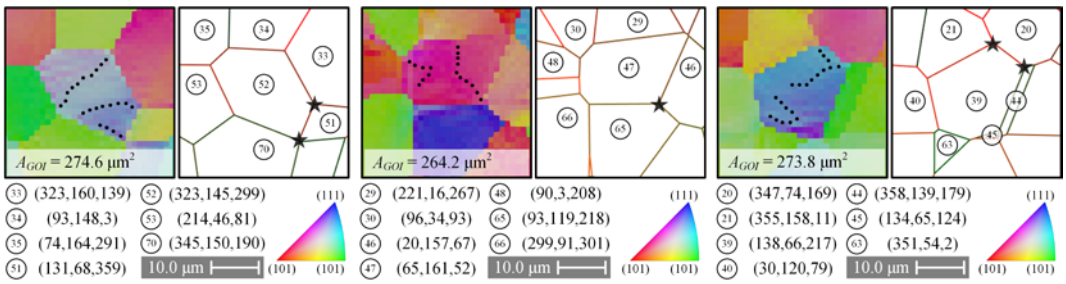

(b)

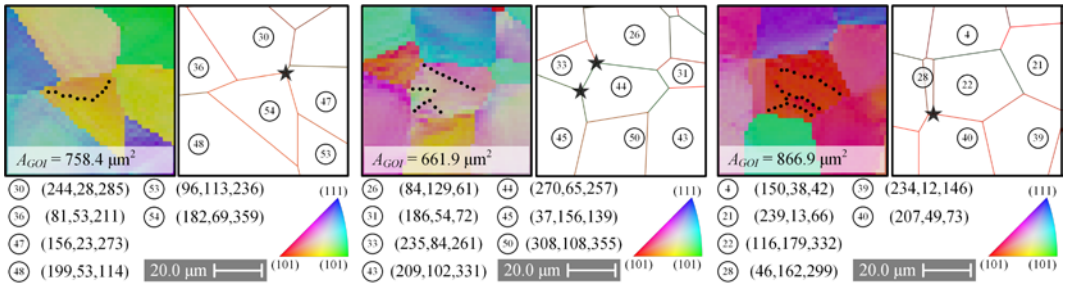

(c)

Fig. 18 Comparison between the qualified TJs obtained by CP and QE: a) FG, b) MG, and c) CG RVEs with pre-strain of 0.11. The IMGBs are denoted by dots in IPFs, and the Euler angles (°) of associated grains are also provided.

Statistical analysis is performed for further comparison. The grain exhibiting IMGBs (IMGB grains) in QE results but presenting no IMGB in CP results is classified as "QE outlier". Similarly, there is also "CP outlier". The remaining grains are denoted as "Match". Although about 10~20% of all IMGB grains are CP outliers, Match grains always take the majority (near 80%) despite of ε_{pre} and $\bar{d}$, as shown in the column sub-graphs in Fig. 19. This manifests that both the QE method and CPFEM simulation provide similar predictions on whether a grain exhibits IMGB. More detailed examination on their consistency is shown in the scatter plots of Fig. 19. Although QE method fails to estimate IMGB pattern (denoted by Mis. Type) or length (with a deviation over 20.0% and denoted by Mis. Length) in several cases, it still presents good agreement with most of the CP results. Moreover, the extracted IMGB lengths in CP results also exhibit linear correlation to A_{GOI}, and the fitted slopes and intercepts are close to experimental results as well.

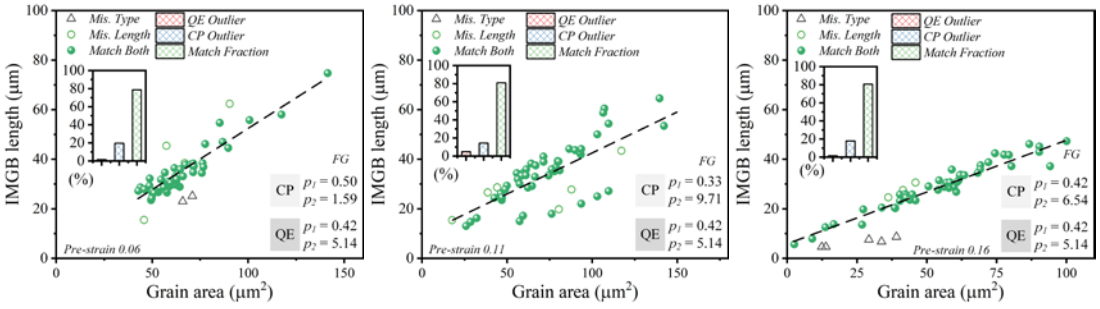

(a1) (a2) (a3)

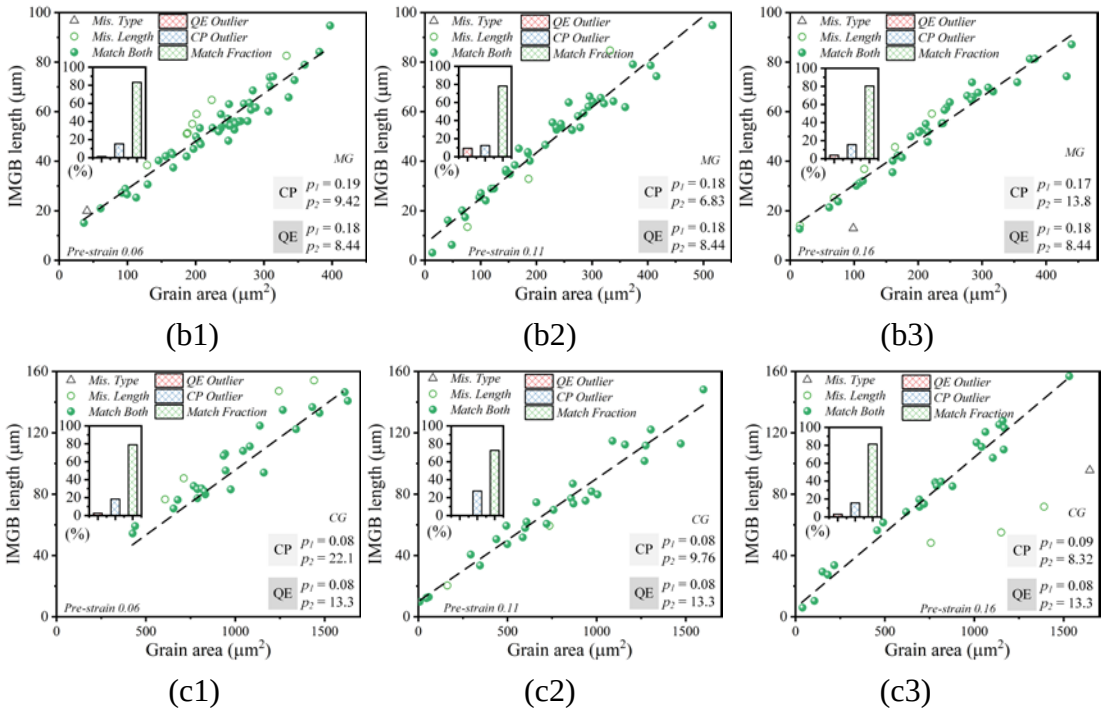

Fig. 19 Statistical analysis on the IMGB information given by CP and QE: results of: a) FG, b) MG, and c) CG. Number 1~3 denotes the pre-strain of 0.06, 0.11, and 0.16, respectively. The slope and intercept are designated as p_1 and p_2.

Above statistical analyses validate the fact that the IMGB information given by CPFEM simulation can be well reproduced by QE method. However, based on the IPFs of CP results, collecting the pattern and length of IMGBs requires the Euler angle extraction and misorientation angle calculation between all adjacent elements in RVEs (Zhang et al., 2022b), which is much more laborious and requires an interruption for data processing before the subsequent SPC deformation simulation. In the contrary, using the experiment-based QE methodology directly yields reliable IMGB information according to the given deforming condition. Therefore, employing the QE method improves not only the computation efficiency of simulation procedure, but also the usefulness of the proposed enhanced constitutive model.

5.2 Evolution analysis on IMGB-induced slip resistance

In the micro-scaled SPC deformation, ε_{pre}, θ_{SPC}, and $\bar{d}$ are commonly used to describe deformation conditions. Compared with the SPC-induced softening and SE-induced coupled facilitation, influences of these three factors on IMGB-induced hardening are much more elusive. Therefore, the evolution of IMGB-induced slip resistance is analyzed with respect to ε_{pre}, θ_{SPC}, and $\bar{d}$ in the grains with representative orientations of (100), (101), and (111).

5.2.1 Effect of pre-strain

Influences of pre-strain on g^{i}_{IMGB} can be explored through the evolution of s_{Mag}. Using the QE methodology, IMGB pattern and magnitude can be determined by Eq. (4) and (21) with presupposed $\bar{d}$ and ε_{pre}, so s_{Mag} can be computed based on the given A_{GOI}. Results of s_{Mag} with respect to $\bar{d}$ and A_{GOI} are plotted as heat maps in Fig. 20, and three levels of pre-strain were used to elucidate its influences. The maximum and average of s_{Mag} are increased from 233.5 and 75.2 MPa to 347.5 and 88.9 MPa, when ε_{pre} is promoted from 0.06 to 0.16. With the increase of pre-strain, the regions denoting none and individual IMGB grains are reduced. The increased fraction of multiple IMGB grains leads to the expansion of areas denoting high s_{Mag}. The possibility for grains exhibiting multiple IMGBs is also increased with ε_{pre}, so the pixels with denser red color are increased in the "to be determined" field (between the yellow and blue dash lines). More severe deformation assists the generation of IMGB and facilitates the pattern transformation from the individual to multiple, leading to the increase of IMGB magnitude and mean misorientation angle. The increased L_{IMGB} and $\bar{\theta}_{Mis}$ both raise the obstruction on incident dislocations while moving across IMGBs, so s_{Mag} is consequently increased with ε_{pre}.

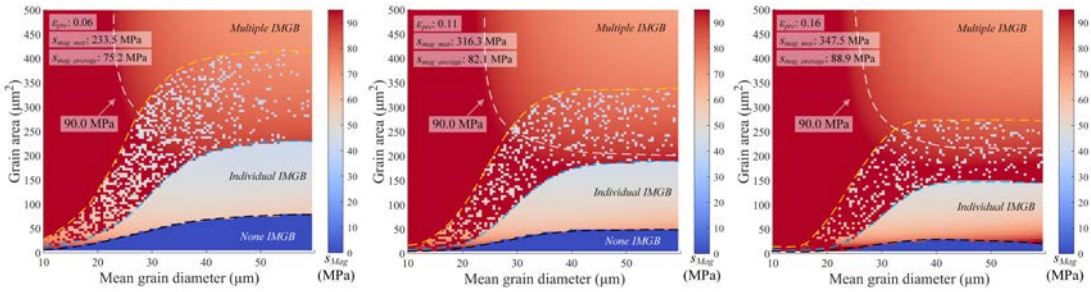

(a) (b) (c)

Fig. 20 The variation of s_{Mag} with pre-strain of: a) 0.06, b) 0.11, and c) 0.16.

5.2.2 Effect of intersection angle

Variation of loading direction leads to the increase of high SF grains, so the influence of θ_{SPC} are analyzed in the evolution of SF for main slip planes. There are four main slip planes, namely $(\bar{1}11)$, $(1\bar{1}1)$, (111), and $(\bar{1}\bar{1}1)$ in FCC lattice, and each maximum SF is plotted with respect to θ_{SPC} in Fig. 21. Owning distinct Euler angles, the shapes of SF evolution curves are divergent although grains exhibiting identical crystallographic orientation. While θ_{SPC} increases from 0 to 90°, the overall maximum

SF may exhibit a wide range. As shown in Fig. 21 (a) and (c), the SFs of (111)-oriented grain and (101)-oriented grain even vary from 0 to 0.5. This warrants the consideration of the distinct activation of each slip plane when modelling the grain-level complex deformation. Moreover, the most favorable slip plane also varies with θ_{SPC}. For the (101)-oriented grain in Fig. 21 (a), its $(1\bar{1}1)$ plane exhibits the maximum SF when θ_{SPC} changes from 0 to 35°. With the increase of θ_{SPC}, $(\bar{1}\bar{1}1)$ plane gradually possesses the maximum SF. However, the (111) plane becomes prone to activation once θ_{SPC} reaches 60°. This suggests that the glide of each slip plane can be moderated via changing the loading direction, so the less activated slip systems can be mobilized in subsequent loading, which eliminates the deformation-induced anisotropy as observed in experiments.

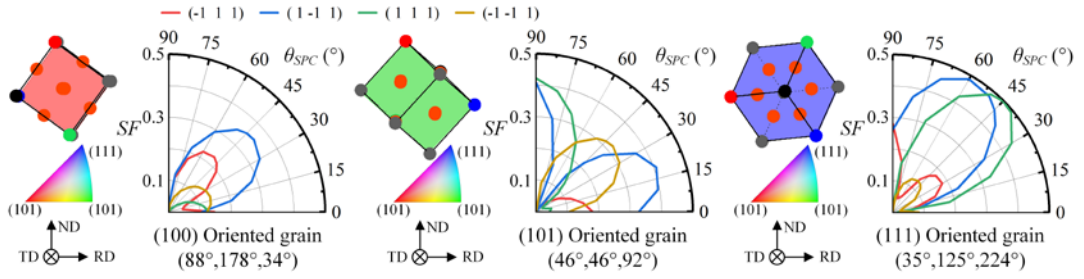

(a)

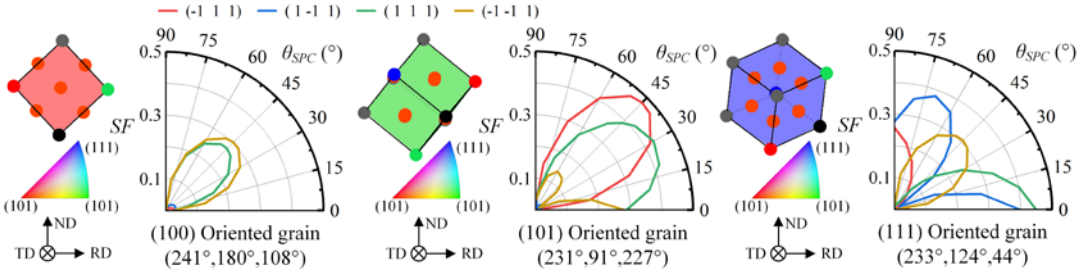

(b)

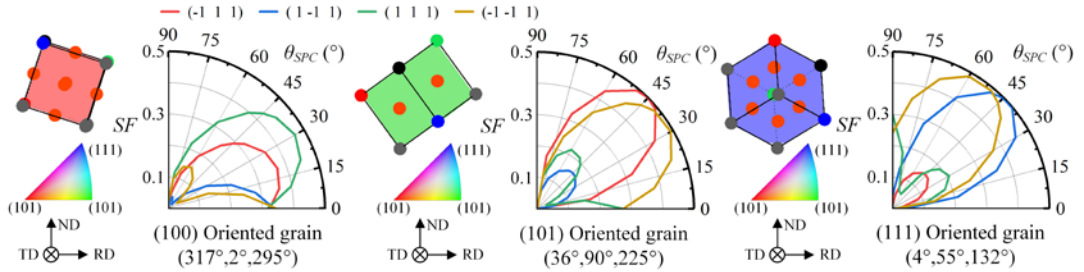

(c)

Fig. 21 Evolution of the maximum SF in each main slip plane with respect to θ_{SPC}: results a) FG, b) MG, and c) CG samples. Grains oriented in (100), (101), and (111) are sequenced from the left to right, respectively.

Results in Fig. 21 validate that SPC loading alters previous SFs and dissimilates the activation extend of each main slip plane. Since θ_{SPC} determines SF in subsequent deformation, it actually governs the interaction intensity between slip planes and IMGB. Therefore, θ_{SPC} mainly influences the first part of g_{IMGB}^{i} in Eq. (13). Unlike the other grains, (100)-oriented grains generally maintain their most favorable slip planes, implying that the sensitivity of g_{IMGB}^{i} to θ_{SPC} is dependent on grain orientation. This orientation dependency also affects the evolution feature of g_{IMGB}^{i} while IMGB pattern transformation, which is further discussed in the following section.

5.2.3 Effect of grain size

To elucidate the influences of grain size on the evolution of g_{IMGB}^{i}, specific grain areas of FG, MG, and CG samples must be given in advance, and IMGB pattern also needs to be presupposed. As such, individual IMGB is assumed to be parallel to the vertical direction in observation plane. Generally, individual IMGB is favored by smaller grains and larger grains tend to exhibit multiple IMGBs (Li et al., 2022b; Zhang et al., 2022b). Results of g_{IMGB}^{i} are plotted with respect to θ_{SPC} in Fig. 22. In each subfigure, the upper and lower row represents the results of small and large IMGB grains, respectively.

As shown in Fig. 22 (a), $(\bar{1}\bar{1}1)$ plane bears relatively low g_{IMGB}^{i} in small grains, but its g_{IMGB}^{i} becomes the highest in the coarsened grains. Similar variation can be found in other cases, such as the $(\bar{1}11)$ plane of (101)-oriented grain in Fig. 22 (b) and the $(1\bar{1}1)$ plane of (111)-oriented grain in Fig. 22 (c). This shows that slip planes with few impedance in small grains can be strongly retarded in large grains, because of the concomitant IMGB pattern transformation (triggered by grain enlargement) from the individual to the multiple. The overall increase of g_{IMGB}^{i} is mainly ascribed to the fact that φ_i reaches 90° once multiple IMGBs are formed in large grains. The drastic increase of slip resistance is obvious in (101)- and (111)-oriented grains but not significant for (100)-oriented grains. Following the sequence of descending g_{IMGB}^{i}, the order of (100)-oriented grains is scarcely affected by grain coarsening. This is attributed to the fact that the most favorable slip planes of (100)-oriented grains nearly remain the same while changing θ_{SPC}, which limits SF variation and hence restrains the alteration of slip plane with the maximum g_{IMGB}^{i}.

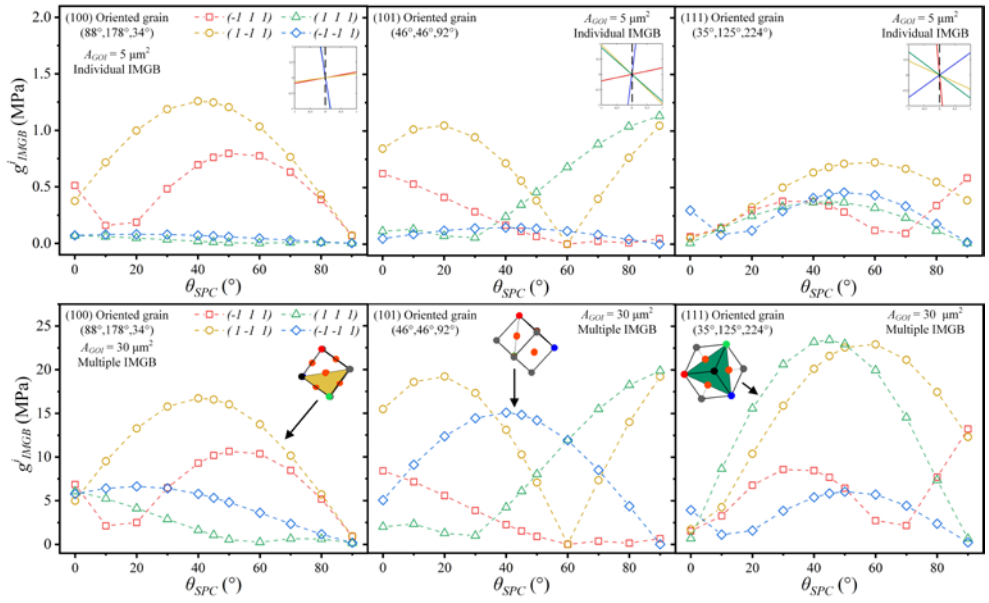
(100) Oriented grain
(88°,178°,34°)
A_{GOI} = 5 μm²
Individual IMGB
(101) Oriented grain
(46°,46°,92°)
(111) Oriented grain
(35°,125°,224°)
A_{GOI} = 30 μm²
Multiple IMGB
g^{I}_{IMGB} (MPa)
θ_{SPC} (°)

(a)

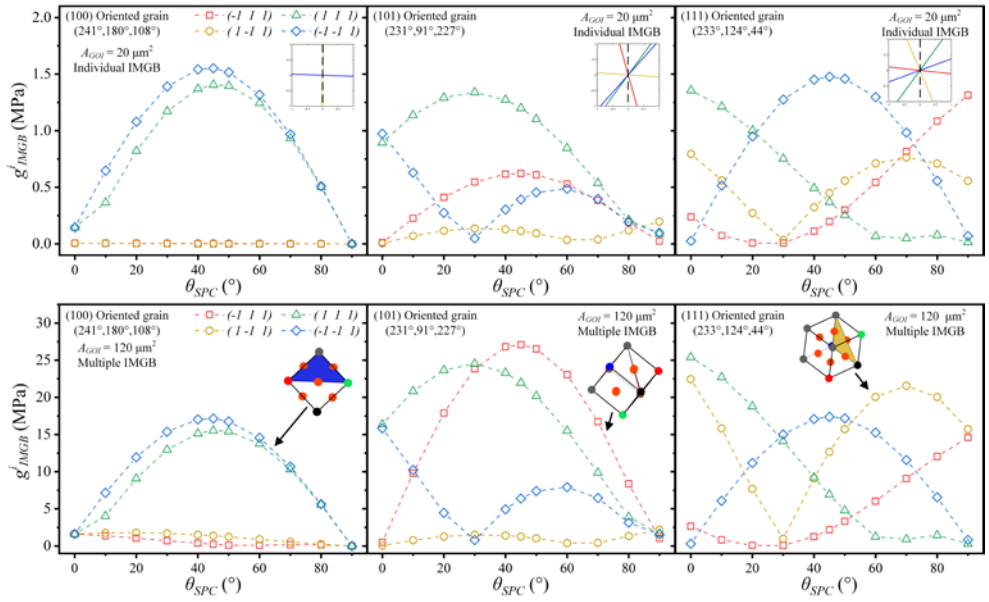
(100) Oriented grain
(241°,180°,108°)
A_{GOI} = 20 μm²
Individual IMGB
(101) Oriented grain
(231°,91°,227°)
(111) Oriented grain
(233°,124°,44°)
A_{GOI} = 120 μm²
Multiple IMGB
g^{I}_{IMGB} (MPa)
θ_{SPC} (°)

(b)

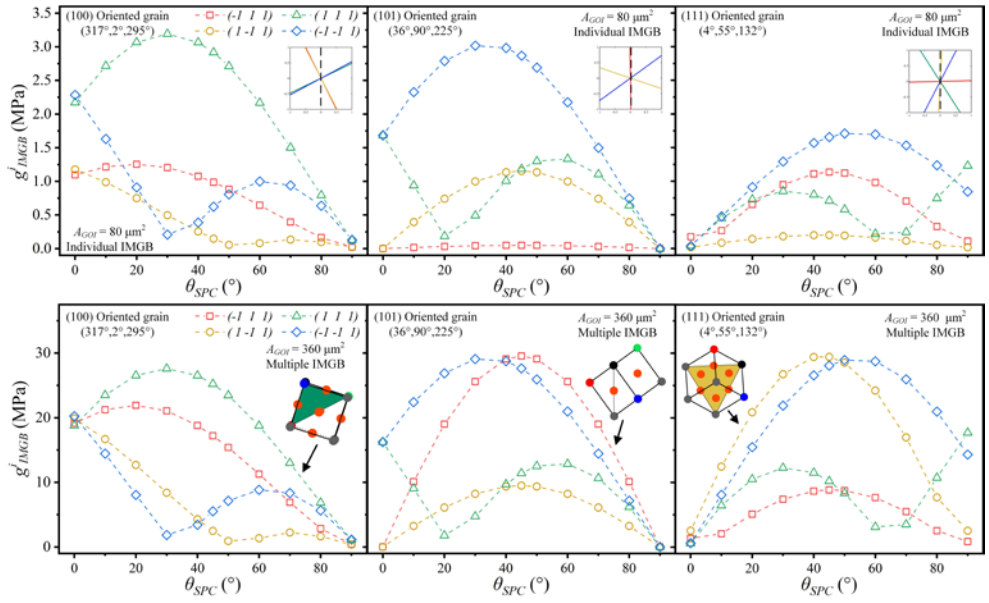

(c)

Fig. 22 Evolution of IMGB-induced slip resistance in each main slip plane with respect to θ_{SPC}: a) FG, b) MG, and c) CG samples. The assumed individual IMGB is represented by the black dash line in sub-windows, and spatial attitudes of the slip planes are also provided.

Based on the data presented in Fig. 22, g^{GOI}_{IMGB} of all four slip planes is computed. As shown in Fig. 23, despite of the mean grain size and Euler angle, curves obtained in multiple IMGB conditions (with legend of "Mul.") are universally much higher, implying that the contribution to increasing overall deformation resistance is mainly dependent on the quantity of grains with multiple IMGBs. The mean of each "Mul." curves are further computed and presented in sub-windows, showing that the (101)- and (111)- oriented grains generally exhibit higher g^{GOI}_{IMGB}. It is interesting to find that g^{GOI}_{IMGB} generally reaches the peak when θ_{SPC} is near 45°. This explains the phenomenon that the greatest r-values are usually obtained while the θ_{SPC} is around 45° (Ha et al., 2013; Zhang et al., 2021b). Grains along thickness direction (ND) are much fewer than those in other dimensions, so the thickness strain is mainly accommodated by intragranular deformation rather than intergranular mode. Previous RD stretching results in the orientation concentration near (101), and subsequent tension along DD further raises the overall g^i_{IMGB}, so both aspects significantly promote the deformation resistance of grains in ND. Therefore, the thickness strain of pre-stretched samples is small in SPC tension along DD, resulting in relatively great Lankford coefficients.

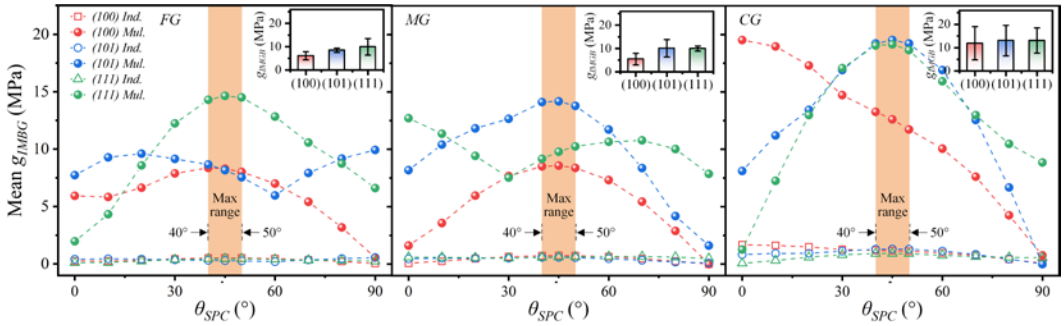

Fig. 23 The average IMGB-induced slip resistance in grains with different IMGB pattern. Sub-windows present the mean of results obtained in multiple IMGB conditions.

6. Conclusions

Two-stage tensile tests using samples with different mean grain sizes were conducted to investigate and model the micro-scaled SPC deformation of ultra-thin sheets. Based on the micro-scaled deformation mechanisms, the IMGB-induced hardening, SPC-induced softening, and SE-induced coupled facilitations are modelled and used to improve conventional CP constitutive model. The methodology for quantitatively estimating IMGB pattern and magnitude, the proposed CPFEM simulation procedure, and the established constitutive model, are validated to well predict the IMGB, flow stress, and microstructure characteristics' evolution in micro-scaled SPC deformation. Some concluding remarks can be drawn in this study:

1) Sample coarsening contributes to the overall decrease of flow stress. Comparing with monotonic tensile results at the same ε_{pre}, the yield stress and hardening rate in subsequent SPC tension are reduced. Increasing ε_{pre} and θ_{SPC} facilitates the SPC-induced softening which, however, is negatively related to $\bar{d}$.

2) The IMGB pattern and magnitude predicted by the experiment-based QE method are consistent with the results of CPFEM simulation. The IMGB information can thus be directly obtained via QE method rather than laboriously updating the information from simulation.

3) The physical nature of IMGBs raises the saturated slip resistance in subsequent SPC loading. This hardening can be assisted by increasing $\bar{d}$, because IMGBs in large grains generally exhibit complex pattern and greater magnitude, resulting in stronger in-grain hardening.

4) The SPC-induced softening mainly lies in the initial slip resistance in SPC deformation, and arises from the increase of high SF grain fraction which influences can be described based on ε_{pre} and δ_{SPC}. Influences of SE are explicitly involved in

the expression of g_{0_SPC} and the determination of fundamental CPFEM parameters.

5) Both the mechanical response and microstructure characteristic evolution in the micro-scaled SPC deformation, are well predicted by the proposed model and simulation scheme. They contribute to advancing the understanding of micro-scaled deformation mechanisms and provide fundamentals for optimizing the multi-stage microforming of ultra-thin sheets for miniaturized parts.

CPFEM is a promising tool for investigating complicated grain-level deformation of polycrystals and the grains locally exhibit multi-axial stress state under external loading. Based on the related literature reports in recent years, this study used the uniaxial stress state assumption for analysis. With the help of more advanced characterization techniques, grains' accurate stress states might be measured in the future, and the work of this study can then be improved by considering more specific and complex situations locally.

Acknowledgements

The authors would like to acknowledge the funding support from the National Natural Science Foundation of China No. 51835011, the Natural Science Foundation of Shanghai (Grant No. 19ZR1425700), and the Shanghai Academy of Spaceflight Technology (USCAST2020-3). This work was also supported by the project of No. SB2V-P0031822 from the Hong Kong Polytechnic University.

Appendix A

The procedure of quantitatively estimating IMGB pattern and magnitude (Zhang et al., 2022b) is illustrated in Fig. A1. The datasets of GeFs and DeFs of each TJ for all grains in observation section can be established based on the RVE. The bounds of GeFs and DeFs are provided in Fig. A2 (a-c) and Eq. (3), which are used to check out whether current GOI exhibits qualified TJs for generating IMGBs. As shown in Fig. A2 (d), area examination in the screened grains is used to determine IMGB pattern. Notably, if A_{GOI} falls in the to-be-determined region, additional determination is needed. IMGB length is computed by using its linear correlation to A_{GOI} as shown in Fig. A1 (c).

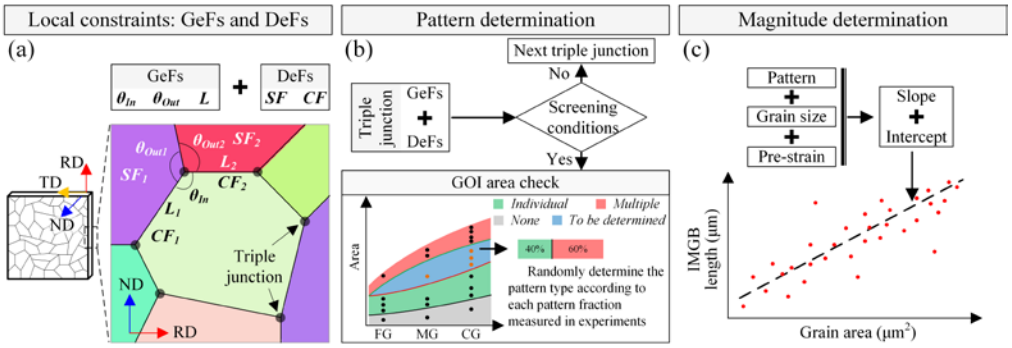

Fig. A1 Schematic of the methodology for estimating IMGB pattern and magnitude: a) definitions of GeFs and DeFs; b) screening qualified TJs via examining local constraints and determining IMGB pattern by checking GOI area; and c) calculating IMGB length by using the linear relationship.

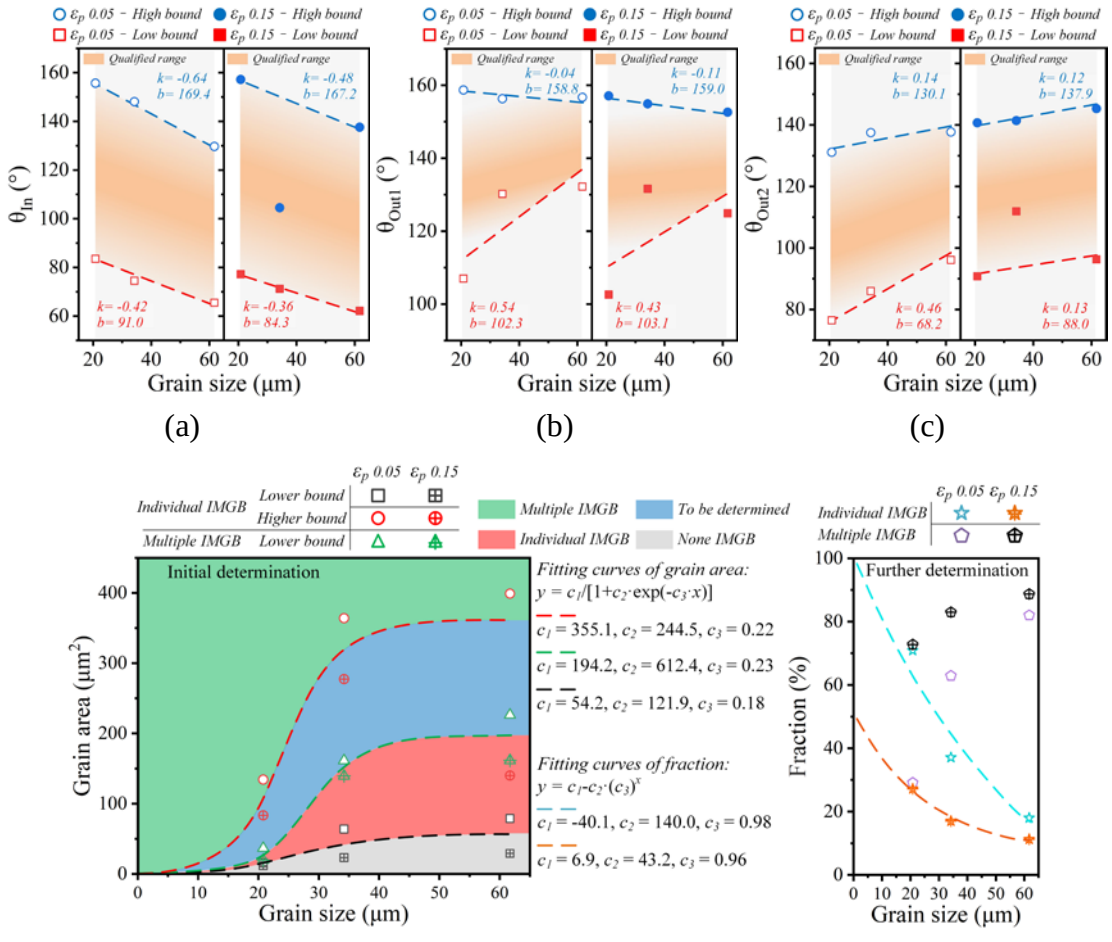

Fig. A2 Explicit expressions for determining the angle bounds and patterns: the linear correlations with $\bar{d}$ for a) θ_{In}, b) θ_{Out1}, and c) θ_{Out2}; and d) the grain-area-based exponential correlations used for IMGB pattern determination.

Potential IMGB pattern and magnitude in each grain under certain deformation

conditions can be evaluated via this QE method. All coefficients needed in the QE procedure are listed in Table A1.

Table A1 The coefficients needed by the QE method.

GeF	Bound	k (°/μm)	b (°)	A_{Bound} (μm^2)	Bound	c_{A1}	c_{A2}	c_{A3}	c_{A4}
θ_{In}	Lower	-0.39	87.7	Individual	Lower	54.2	121.9	0.18	1.0
	Upper	-0.56	168.3		Upper	355.1	244.5	0.23	3.0
θ_{Out1}	Lower	0.49	102.7	Multiple	Lower	194.2	612.4	0.22	1.5
	Upper	0.08	158.9	$F_{Pattern}$ (%)	ε_p	c_{F1}	c_{F2}	c_{F3}	-
θ_{Out2}	Lower	0.30	78.1	Individual	0.05	-40.1	140.0	0.98	-
	Upper	0.13	134.0		0.15	6.9	43.2	0.96	-

Appendix B

The SPC parameter δ_{SPC} is employed to describe the coupled effects of deformation-induced anisotropy and loading direction variation. For the former one, Lankford coefficient ($r_{\theta_{SPC}}$) is computed as:

$$r_{\theta_{SPC}} = -\left(\varepsilon_b/\varepsilon_l\right)/\left(1+\varepsilon_b/\varepsilon_l\right) \tag{B1}$$

where ε_b and ε_l are the true strain along the transverse and longitude direction while stretching. The SPC parameter is defined as:

$$\delta_{SPC} = \left(\dot{\mathbf{E}}_{\mathbf{pre}} : \dot{\mathbf{E}}_{\mathbf{sub}}\right)/\left(\left\|\dot{\mathbf{E}}_{\mathbf{pre}}\right\|\left\|\dot{\mathbf{E}}_{\mathbf{sub}}\right\|\right) \tag{B2}$$

where $\dot{\mathbf{E}}_{\mathbf{pre}}$ and $\dot{\mathbf{E}}_{\mathbf{sub}}$ are the rate of plastic deformation tensor of previous and subsequent tension. This tensor is calculated based on $r_{\theta_{SPC}}$ and θ_{SPC} as:

$$\dot{\mathbf{E}}_{\boldsymbol{\theta}_{\mathbf{SPC}}} = \dot{\varepsilon}_{\theta_{SPC}} \begin{bmatrix} \cos^2\theta_{SPC} - \sin^2\theta_{SPC}\cdot r_{\theta_{SPC}}/\left(1+r_{\theta_{SPC}}\right) & \cos\theta_{SPC}\sin\theta_{SPC}\cdot\left(1+2r_{\theta_{SPC}}\right)/\left(1+r_{\theta_{SPC}}\right) & 0 \\ \cos\theta_{SPC}\sin\theta_{SPC}\cdot\left(1+2r_{\theta_{SPC}}\right)/\left(1+r_{\theta_{SPC}}\right) & \sin^2\theta_{SPC} - \cos^2\theta_{SPC}\cdot r_{\theta_{SPC}}/\left(1+r_{\theta_{SPC}}\right) & 0 \\ 0 & 0 & -1/\left(1+r_{\theta_{SPC}}\right) \end{bmatrix} \tag{B3}$$

According to previous study (Zhang et al., 2021b), the SPC parameters obtained in

experiments with different $\bar{d}$, ε_{pre}, and θ_{SPC} are plotted in Fig. B1. δ_{SPC} is insensitive to $\bar{d}$ and ε_{pre}, but is linearly correlated to θ_{SPC} (rad) as:

$$\delta_{SPC} = 1.0 - 0.91 \cdot \theta_{SPC} \tag{B4}$$

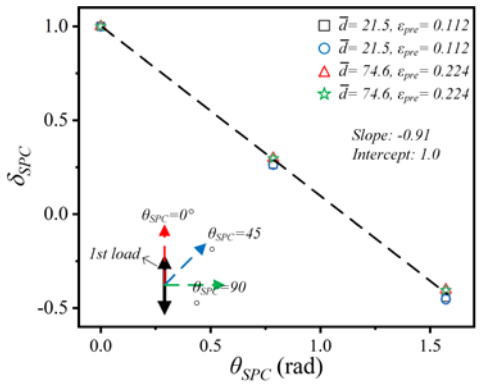

Fig. B1 The linear relationship between the SPC parameter and intersection angle.

Appendix C

The loading conditions in CPFEM simulation are expressed by the deformation gradient rate tensor ($\dot{\mathbf{F}}$) and virtual loading time (t) (Zhang et al., 2018). Previous stretching along X for strain of 0.10 and the second stage tension along Y for strain of 0.05 can be respectively represented as:

$$\dot{\mathbf{F}} = \begin{bmatrix} 1.0\text{x}10^{-4} & 0 & 0 \\ 0 & * & 0 \\ 0 & 0 & * \end{bmatrix}, \quad t = 1000, \quad \dot{\mathbf{F}} = \begin{bmatrix} * & 0 & 0 \\ 0 & 1.0\text{x}10^{-4} & 0 \\ 0 & 0 & * \end{bmatrix}, \quad t = 500 \tag{C1}$$

where the asterisk (*) implies that the corresponding component of the first Piola-Kirchhoff stress tensor is enforced to be zero (Zhang et al., 2018).

Fundamental parameters that mainly influence the yield stress in CPFEM simulation are systematically investigated through the simulation attempts with conditions listed in Table C1. The Mises stress associated with strain of 0.006 is taken as the yield stress in simulation. A variation rate defined as the ratio between the current and minimum value (in each range) of a certain parameter is used to quantify the variation extend. The yield stress given by simulation is plotted with respect to the variation rate of g_0 in Fig. C1 (a). Although the variation rate of g_s and h_0 are over 1.4 in some cases, the yield stress keeps relatively steady. Simulation yield stress is strongly dependent on g_0, as the alternation of g_0 drastically changes the results. Further plotting the experimental yield stress with respect to the associated g_0 (listed in Table 2) in Fig. C1 (b), the correlation

between yield stress σ_{yield} and g_0 can thus be approximated by:

$$\sigma_{yield} = c_1 + c_2 * g_0 \quad \text{(C2)}$$

This correlation is valid for austenite SS 316L, and specific relationship for other materials can be determined similarly.

Table C1 Conditions for yield stress study in CPFEM simulation.

Range Num.	g_0 (MPa)	g_s (MPa)	h_0 (MPa)
Range1	50	350	250
	75	550	350
	100	750	450
Range2	125	350	250
	150	550	350
	175	750	450
Range3	125	850	550
	150	1050	650
	175	1250	750

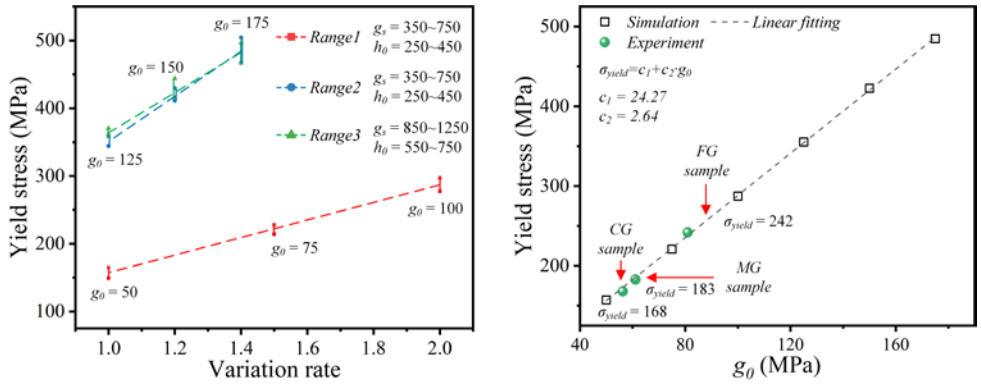

(a) (b)

Fig. C1 Correlation between yield stress and fundamental parameters of CPFEM simulation: a) the evolution of yield stress, and b) the linear correlation between yield stress and g_0.

Reference

Armstrong, R.W., 1961. On size effects in polycrystal plasticity. Journal of the Mechanics and Physics of Solids 9, 196-199. https://doi.org/10.1016/0022-5096(61)90018-7

Asaro, R.J., Needleman, A., 1985. Overview no. 42 Texture development and strain hardening in rate dependent polycrystals. Acta Metallurgica 33, 923-953. https://doi.org/10.1016/0001-6160(85)90188-9

Ashby, M.F., 1970. The deformation of plastically non-homogeneous materials. The

Philosophical Magazine: A Journal of Theoretical Experimental and Applied Physics 21, 399-424. 10.1080/14786437008238426
Barlat, F., Glazov, M.V., Brem, J.C., Lege, D.J., 2002. A simple model for dislocation behavior, strain and strain rate hardening evolution in deforming aluminum alloys. International Journal of Plasticity 18, 919-939. https://doi.org/10.1016/S0749-6419(01)00015-8
Barlat, F., Gracio, J.J., Lee, M.-G., Rauch, E.F., Vincze, G., 2011. An alternative to kinematic hardening in classical plasticity. International Journal of Plasticity 27, 1309-1327. https://doi.org/10.1016/j.ijplas.2011.03.003
Barlat, F., Vincze, G., Grácio, J.J., Lee, M.G., Rauch, E.F., Tomé, C.N., 2014. Enhancements of homogenous anisotropic hardening model and application to mild and dual-phase steels. International Journal of Plasticity 58, 201-218. https://doi.org/10.1016/j.ijplas.2013.11.002
Bong, H.J., Lee, J., Kim, J.-H., Barlat, F., Lee, M.-G., 2017. Two-stage forming approach for manufacturing ferritic stainless steel bipolar plates in PEM fuel cell: Experiments and numerical simulations. International Journal of Hydrogen Energy 42, 6965-6977. https://doi.org/10.1016/j.ijhydene.2016.12.094
Chen, S., Liao, J., Xiang, H., Xue, X., Pereira, A.B., 2021. Pre-strain effect on twist springback of a 3D P-channel in deep drawing. Journal of Materials Processing Technology 287, 116224. https://doi.org/10.1016/j.jmatprotec.2019.05.005
Chen, S., Yu, Q., 2019. The role of low angle grain boundary in deformation of titanium and its size effect. Scripta Materialia 163, 148-151. https://doi.org/10.1016/j.scriptamat.2018.10.054
Chun, B.K., Jinn, J.T., Lee, J.K., 2002. Modeling the Bauschinger effect for sheet metals, part I: theory. International Journal of Plasticity 18, 571-595. https://doi.org/10.1016/S0749-6419(01)00046-8
Crystal, I.R., Schuh, C.A., 2021. Grain-size effect on cracking accumulation in yttria-doped zirconia ceramics during cyclic martensitic transformations. Acta Materialia 209, 116789. https://doi.org/10.1016/j.actamat.2021.116789
Engel, U., Eckstein, R., 2002. Microforming—from basic research to its realization. Journal of Materials Processing Technology 125-126, 35-44. https://doi.org/10.1016/S0924-0136(02)00415-6
Frodal, B.H., Dæhli, L.E.B., Børvik, T., Hopperstad, O.S., 2019. Modelling and simulation of ductile failure in textured aluminium alloys subjected to compression-tension loading. International Journal of Plasticity 118, 36-69. https://doi.org/10.1016/j.ijplas.2019.01.008
Fu, M.W., Chan, W.L., 2013. A review on the state-of-the-art microforming technologies. The International Journal of Advanced Manufacturing Technology 67, 2411-2437. 10.1007/s00170-012-4661-7
Geiger, M., Kleiner, M., Eckstein, R., Tiesler, N., Engel, U., 2001. Microforming. CIRP Annals 50, 445-462. https://doi.org/10.1016/S0007-8506(07)62991-6
Guan, D., Wynne, B., Gao, J., Huang, Y., Rainforth, W.M., 2019. Basal slip mediated tension twin variant selection in magnesium WE43 alloy. Acta Materialia 170, 1-14.

https://doi.org/10.1016/j.actamat.2019.03.018
Guo, N., Wang, J., Sun, C.Y., Zhang, Y.F., Fu, M.W., 2020. Analysis of size dependent earing evolution in micro deep drawing of TWIP steel by using crystal plasticity modeling. International Journal of Mechanical Sciences 165, 105200. https://doi.org/10.1016/j.ijmecsci.2019.105200
Ha, J., Lee, J., Kim, J.H., Lee, M.-G., Barlat, F., 2017. Investigation of plastic strain rate under strain path changes in dual-phase steel using microstructure-based modeling. International Journal of Plasticity 93, 89-111. https://doi.org/10.1016/j.ijplas.2017.02.005
Ha, J., Lee, M.-G., Barlat, F., 2013. Strain hardening response and modeling of EDDQ and DP780 steel sheet under non-linear strain path. Mechanics of Materials 64, 11-26. https://doi.org/10.1016/j.mechmat.2013.04.004
Hall, E.O., 1951. The Deformation and Ageing of Mild Steel: III Discussion of Results. Proceedings of the Physical Society. Section B 64, 747. 10.1088/0370-1301/64/9/303
Hama, T., Yagi, S., Tatsukawa, K., Maeda, Y., Maeda, Y., Takuda, H., 2021. Evolution of plastic deformation behavior upon strain-path changes in an A6022-T4 Al alloy sheet. International Journal of Plasticity 137, 102913. https://doi.org/10.1016/j.ijplas.2020.102913
Harte, A., Atkinson, M., Preuss, M., Quinta da Fonseca, J., 2020. A statistical study of the relationship between plastic strain and lattice misorientation on the surface of a deformed Ni-based superalloy. Acta Materialia 195, 555-570. https://doi.org/10.1016/j.actamat.2020.05.029
He, W., Lin, T., Liu, Q., 2018. Experiments and constitutive modeling of deformation behavior of a magnesium sheet during two-step loading. International Journal of Solids and Structures 147, 52-60. https://doi.org/10.1016/j.ijsolstr.2018.04.009
Hémery, S., Villechaise, P., 2019. In situ EBSD investigation of deformation processes and strain partitioning in bi-modal Ti-6Al-4V using lattice rotations. Acta Materialia 171, 261-274. https://doi.org/10.1016/j.actamat.2019.04.033
Hérault, D., Thuillier, S., Lee, S.-Y., Manach, P.-Y., Barlat, F., 2021. Calibration of a strain path change model for a dual phase steel. International Journal of Mechanical Sciences 194, 106217. https://doi.org/10.1016/j.ijmecsci.2020.106217
Holmedal, B., Houtte, P.V., An, Y., 2008. A crystal plasticity model for strain-path changes in metals. International Journal of Plasticity 24, 1360-1379. https://doi.org/10.1016/j.ijplas.2007.09.007
Keller, C., Hug, E., 2017. Kocks-Mecking analysis of the size effects on the mechanical behavior of nickel polycrystals. International Journal of Plasticity 98, 106-122. https://doi.org/10.1016/j.ijplas.2017.07.003
Kim, K.H., Yin, J.J., 1997. Evolution of anisotropy under plane stress. Journal of the Mechanics and Physics of Solids 45, 841-851. https://doi.org/10.1016/S0022-5096(96)00085-3
Lai, X., Peng, L., Hu, P., Lan, S., Ni, J., 2008. Material behavior modelling in micro/meso-scale forming process with considering size/scale effects. Computational

Materials Science 43, 1003-1009. https://doi.org/10.1016/j.commatsci.2008.02.017
Lee, J., Kim, D., Lee, Y.S., Bong, H.J., Barlat, F., Lee, M.G., 2015. Stress update algorithm for enhanced homogeneous anisotropic hardening model. Computer Methods in Applied Mechanics and Engineering 286, 63-86. https://doi.org/10.1016/j.cma.2014.12.016
Li, L., Liu, L., Shibutani, Y., 2022a. Defect interaction summary between edge dislocations and <112>-axis symmetric tilt grain boundaries in copper on activation barriers and critical stresses. International Journal of Plasticity 149, 103153. https://doi.org/10.1016/j.ijplas.2021.103153
Li, W.T., Li, H., Fu, M.W., 2019. Interactive effect of stress state and grain size on fracture behaviours of copper in micro-scaled plastic deformation. International Journal of Plasticity 114, 126-143. https://doi.org/10.1016/j.ijplas.2018.10.013
Li, Y., Zhang, H., Shang, X., Liu, M., Zhao, S., Cui, Z., 2022b. A multiscale investigation on the preferential deformation mechanism of coarse grains in the mixed-grain structure of 316LN steel. International Journal of Plasticity 152, 103244. https://doi.org/10.1016/j.ijplas.2022.103244
Liao, J., Sousa, J.A., Lopes, A.B., Xue, X., Barlat, F., Pereira, A.B., 2017. Mechanical, microstructural behaviour and modelling of dual phase steels under complex deformation paths. International Journal of Plasticity 93, 269-290. https://doi.org/10.1016/j.ijplas.2016.03.010
Mánik, T., Holmedal, B., Hopperstad, O.S., 2015. Strain-path change induced transients in flow stress, work hardening and r-values in aluminum. International Journal of Plasticity 69, 1-20. https://doi.org/10.1016/j.ijplas.2015.01.004
Mecking, H., Kocks, U.F., 1981. Kinetics of flow and strain-hardening. Acta Metallurgica 29, 1865-1875. https://doi.org/10.1016/0001-6160(81)90112-7
Parkin, J., Birosca, S., 2021. Crystallographic orientation influence on slip system activation and deformation mechanisms in Waspaloy during in-situ mechanical loading. Journal of Alloys and Compounds 865, 158548. https://doi.org/10.1016/j.jallcom.2020.158548
Peirce, D., Asaro, R.J., Needleman, A., 1982. An analysis of nonuniform and localized deformation in ductile single crystals. Acta Metallurgica 30, 1087-1119. https://doi.org/10.1016/0001-6160(82)90005-0
Peng, L., Yi, P., Lai, X., 2014. Design and manufacturing of stainless steel bipolar plates for proton exchange membrane fuel cells. International Journal of Hydrogen Energy 39, 21127-21153. https://doi.org/10.1016/j.ijhydene.2014.08.113
Peng, L.F., Mao, M.Y., Fu, M.W., Lai, X.M., 2016. Effect of grain size on the adhesive and ploughing friction behaviours of polycrystalline metals in forming process. International Journal of Mechanical Sciences 117, 197-209. https://doi.org/10.1016/j.ijmecsci.2016.08.022
Petch, N.J., 1953. The cleavage strength of polycrystals. Journal of the Iron and Steel Institute 174, 25-28.
Qin, J., Holmedal, B., Hopperstad, O.S., 2019. Experimental characterization and modeling of aluminum alloy AA3103 for complex single and double strain-path

changes. International Journal of Plasticity 112, 158-171. https://doi.org/10.1016/j.ijplas.2018.08.011
Qin, J., Holmedal, B., Zhang, K., Hopperstad, O.S., 2017. Modeling strain-path changes in aluminum and steel. International Journal of Solids and Structures 117, 123-136. https://doi.org/10.1016/j.ijsolstr.2017.03.032
Renault-Laborne, A., Hure, J., Malaplate, J., Gavoille, P., Sefta, F., Tanguy, B., 2018. Tensile properties and deformation microstructure of highly neutron-irradiated 316 stainless steels at low and fast strain rate. Journal of Nuclear Materials 508, 488-504. https://doi.org/10.1016/j.jnucmat.2018.05.068
Robertson, C., Fivel, M.C., Fissolo, A., 2001. Dislocation substructure in 316L stainless steel under thermal fatigue up to 650 K. Materials Science and Engineering: A 315, 47-57. https://doi.org/10.1016/S0921-5093(01)01201-1
Roters, F., Diehl, M., Shanthraj, P., Eisenlohr, P., Reuber, C., Wong, S.L., Maiti, T., Ebrahimi, A., Hochrainer, T., Fabritius, H.O., Nikolov, S., Friák, M., Fujita, N., Grilli, N., Janssens, K.G.F., Jia, N., Kok, P.J.J., Ma, D., Meier, F., Werner, E., Stricker, M., Weygand, D., Raabe, D., 2019. DAMASK – The Düsseldorf Advanced Material Simulation Kit for modeling multi-physics crystal plasticity, thermal, and damage phenomena from the single crystal up to the component scale. Computational Materials Science 158, 420-478. https://doi.org/10.1016/j.commatsci.2018.04.030
Roters, F., Eisenlohr, P., Hantcherli, L., Tjahjanto, D.D., Bieler, T.R., Raabe, D., 2010. Overview of constitutive laws, kinematics, homogenization and multiscale methods in crystal plasticity finite-element modeling: Theory, experiments, applications. Acta Materialia 58, 1152-1211. https://doi.org/10.1016/j.actamat.2009.10.058
Samuel, E.I., Choudhary, B.K., Bhanu Sankara Rao, K., 2002. Influence of temperature and strain rate on tensile work hardening behaviour of type 316 LN austenitic stainless steel. Scripta Materialia 46, 507-512. https://doi.org/10.1016/S1359-6462(02)00023-4
Schlosser, F., Signorelli, J., Leonard, M., Roatta, A., Milesi, M., Bozzolo, N., 2019. Influence of the strain path changes on the formability of a zinc sheet. Journal of Materials Processing Technology 271, 101-110. https://doi.org/10.1016/j.jmatprotec.2019.03.026
Schmitt, J.H., Aernoudt, E., Baudelet, B., 1985. Yield loci for polycrystalline metals without texture. Materials Science and Engineering 75, 13-20. https://doi.org/10.1016/0025-5416(85)90173-9
Sedighiani, K., Shah, V., Traka, K., Diehl, M., Roters, F., Sietsma, J., Raabe, D., 2021. Large-deformation crystal plasticity simulation of microstructure and microtexture evolution through adaptive remeshing. International Journal of Plasticity 146, 103078. https://doi.org/10.1016/j.ijplas.2021.103078
Shang, X., Zhang, H., Cui, Z., Fu, M.W., Shao, J., 2020. A multiscale investigation into the effect of grain size on void evolution and ductile fracture: Experiments and crystal plasticity modeling. International Journal of Plasticity 125, 133-149. https://doi.org/10.1016/j.ijplas.2019.09.009
Sperry, R., Han, S., Chen, Z., Daly, S.H., Crimp, M.A., Fullwood, D.T., 2021.

Comparison of EBSD, DIC, AFM, and ECCI for active slip system identification in deformed Ti-7Al. Materials Characterization 173, 110941. https://doi.org/10.1016/j.matchar.2021.110941
Sun, C.Y., Guo, N., Fu, M.W., Wang, S.W., 2016. Modeling of slip, twinning and transformation induced plastic deformation for TWIP steel based on crystal plasticity. International Journal of Plasticity 76, 186-212. https://doi.org/10.1016/j.ijplas.2015.08.003
Sun, L., Xu, Z., Peng, L., Lai, X., 2022. Grain-size-dependent ductile-to-brittle fracture mechanism of titanium sheets. Scripta Materialia 219, 114877. https://doi.org/10.1016/j.scriptamat.2022.114877
Tang, X.F., Peng, L.F., Shi, S.Q., Fu, M.W., 2019. Influence of crystal structure on size dependent deformation behavior and strain heterogeneity in micro-scale deformation. International Journal of Plasticity 118, 147-172. https://doi.org/10.1016/j.ijplas.2019.02.004
Tang, X.F., Shi, S.Q., Fu, M.W., 2020. Interactive effect of grain size and crystal structure on deformation behavior in progressive micro-scaled deformation of metallic materials. International Journal of Machine Tools and Manufacture 148, 103473. https://doi.org/10.1016/j.ijmachtools.2019.103473
Tasan, C.C., Hoefnagels, J.P.M., Diehl, M., Yan, D., Roters, F., Raabe, D., 2014. Strain localization and damage in dual phase steels investigated by coupled in-situ deformation experiments and crystal plasticity simulations. International Journal of Plasticity 63, 198-210. https://doi.org/10.1016/j.ijplas.2014.06.004
Taylor, G.I., 1934. The mechanism of plastic deformation of crystals. Part I.—Theoretical. Proceedings of the Royal Society of London. Series A, Containing Papers of a Mathematical and Physical Character 145, 362-387. 10.1098/rspa.1934.0106
Thuillier, S., Manach, P.Y., 2009. Comparison of the work-hardening of metallic sheets using tensile and shear strain paths. International Journal of Plasticity 25, 733-751. https://doi.org/10.1016/j.ijplas.2008.07.002
Wen, W., Borodachenkova, M., Tomé, C.N., Vincze, G., Rauch, E.F., Barlat, F., Grácio, J.J., 2015. Mechanical behavior of Mg subjected to strain path changes: Experiments and modeling. International Journal of Plasticity 73, 171-183. https://doi.org/10.1016/j.ijplas.2014.10.009
Wi, M.S., Lee, S.Y., Kim, J.H., Kim, J.M., Barlat, F., 2020. Experimental and theoretical plasticity analyses of steel materials deformed under a nonlinear strain path. International Journal of Mechanical Sciences 182, 105770. https://doi.org/10.1016/j.ijmecsci.2020.105770
Wroński, M., Kumar, M.A., McCabe, R.J., Wierzbanowski, K., Tomé, C.N., 2022. Deformation behavior of CP-titanium under strain path changes: Experiment and crystal plasticity modeling. International Journal of Plasticity 148, 103129. https://doi.org/10.1016/j.ijplas.2021.103129
Wu, X., Suo, H., Ji, Y., Li, J., Ma, L., Liu, M., Zhang, Z., Wang, Q., 2020. Systematical analysis on the grain orientation evolution of pure nickel under plastic deformation by using in-situ EBSD. Materials Science and Engineering: A 792,

139722. https://doi.org/10.1016/j.msea.2020.139722
Xu, Z., Peng, L., Bao, E., 2018. Size effect affected springback in micro/meso scale bending process: Experiments and numerical modeling. Journal of Materials Processing Technology 252, 407-420.
https://doi.org/10.1016/j.jmatprotec.2017.08.040
Xu, Z., Qiu, D., Yi, P., Peng, L., Lai, X., 2020. Towards mass applications: A review on the challenges and developments in metallic bipolar plates for PEMFC. Progress in Natural Science: Materials International 30, 815-824.
https://doi.org/10.1016/j.pnsc.2020.10.015
Xu, Z.T., Peng, L.F., Fu, M.W., Lai, X.M., 2015. Size effect affected formability of sheet metals in micro/meso scale plastic deformation: Experiment and modeling. International Journal of Plasticity 68, 34-54.
https://doi.org/10.1016/j.ijplas.2014.11.002
Yoshida, F., Uemori, T., Fujiwara, K., 2002. Elastic–plastic behavior of steel sheets under in-plane cyclic tension–compression at large strain. International Journal of Plasticity 18, 633-659. https://doi.org/10.1016/S0749-6419(01)00049-3
Zaman, S.B., Barlat, F., Kim, J.-H., 2018. Deformation-induced anisotropy of uniaxially prestrained steel sheets. International Journal of Solids and Structures 134, 20-29. https://doi.org/10.1016/j.ijsolstr.2017.10.029
Zhang, D., Li, H., Guo, X., Yang, Y., Yang, X., Feng, Z., 2022a. An insight into size effect on fracture behavior of Inconel 718 cross-scaled foils. International Journal of Plasticity 153, 103274. https://doi.org/10.1016/j.ijplas.2022.103274
Zhang, H., Liu, J., Sui, D., Cui, Z., Fu, M.W., 2018. Study of microstructural grain and geometric size effects on plastic heterogeneities at grain-level by using crystal plasticity modeling with high-fidelity representative microstructures. International Journal of Plasticity 100, 69-89. https://doi.org/10.1016/j.ijplas.2017.09.011
Zhang, R., Lan, S., Xu, Z., Qiu, D., Peng, L., 2021a. Investigation and optimization of the ultra-thin metallic bipolar plate multi-stage forming for proton exchange membrane fuel cell. Journal of Power Sources 484, 229298.
https://doi.org/10.1016/j.jpowsour.2020.229298
Zhang, R., Xu, Z., Deng, Y., Peng, L., 2020a. Characterizing the back stress of ultra-thin metallic sheet via pre-strain tension/bending process. Journal of Materials Processing Technology 279, 116560.
https://doi.org/10.1016/j.jmatprotec.2019.116560
Zhang, R., Xu, Z., Peng, L., Lai, X., Fu, M.W., 2021b. Modelling of ultra-thin steel sheet in two-stage tensile deformation considering strain path change and grain size effect and application in multi-stage microforming. International Journal of Machine Tools and Manufacture 164, 103713.
https://doi.org/10.1016/j.ijmachtools.2021.103713
Zhang, R., Xu, Z., Peng, L., Lai, X., Fu, M.W., 2022b. Intragranularly misoriented grain boundary evolution affected by local constraints and grain size in micro-scale deformation of ultra-thin metallic sheets. International Journal of Plasticity 157, 103377. https://doi.org/10.1016/j.ijplas.2022.103377

Zhang, S., Liu, W., Wan, J., Misra, R.D.K., Wang, Q., Wang, C., 2020b. The grain size and orientation dependence of geometrically necessary dislocations in polycrystalline aluminum during monotonic deformation: Relationship to mechanical behavior. Materials Science and Engineering: A 775, 138939. https://doi.org/10.1016/j.msea.2020.138939
Zheng, J.-Y., Fang, J.Y.C., Fu, M.W., 2022. Flow-induced folding in multi-scaled bulk forming of axisymmetric flanged parts and its prediction and avoidance. The International Journal of Advanced Manufacturing Technology 119, 5863-5883. 10.1007/s00170-021-08382-8
Zheng, J.-Y., Shi, S.Q., Fu, M.W., 2020. Progressive microforming of pin-shaped plunger parts and the grain size effect on its forming quality. Materials & Design 187, 108386. https://doi.org/10.1016/j.matdes.2019.108386